OPEN ACCESS

University of BRISTOL

Witttman, S., Abdala, A. P., & Rubin, J. E. (2019). Reduced computational modelling of Kölliker-Fuse contributions to breathing patterns in Rett syndrome. *Journal of Physiology*, *597*(10), 2651-2672. https://doi.org/10.1113/JP277592

Peer reviewed version

Link to published version (if available):
10.1113/JP277592

Link to publication record in Explore Bristol Research
PDF-document

This is the author accepted manuscript (AAM). The final published version (version of record) is available online via Wiley at https://physoc.onlinelibrary.wiley.com/doi/full/10.1113/JP277592 . Please refer to any applicable terms of use of the publisher.

University of Bristol - Explore Bristol Research
General rights

This document is made available in accordance with publisher policies. Please cite only the published version using the reference above. Full terms of use are available:
http://www.bristol.ac.uk/red/research-policy/pure/user-guides/ebr-terms/

Reduced computational modeling of Kölliker-Fuse contributions to breathing patterns in Rett syndrome

Samuel Wittman*
Department of Mathematics
University of Pittsburgh

Ana Paula Abdala†
School of Physiology, Pharmacology & Neuroscience
Faculty of Life Sciences
University of Bristol
Biomedical Sciences Building
University Walk
Bristol BS8 1TD
United Kingdom

Jonathan E. Rubin‡
Department of Mathematics &
Center for the Neural Basis of Cognition
University of Pittsburgh
301 Thackeray Hall
Pittsburgh, PA 15260, USA

February 18, 2019

*srw52@pitt.edu
†Ana.Abdala@bristol.ac.uk
‡jonrubin@pitt.edu

Abstract

Rett syndrome (RTT) is a developmental disorder that can lead to respiratory disturbances featuring prolonged apneas of variable durations. Determining the mechanisms underlying these effects at the level of respiratory neural circuits would have significant implications for treatment efforts and would also enhance our understanding of respiratory rhythm generation and control. While experimental studies have suggested possible factors contributing to the respiratory patterns of RTT, we take a novel computational approach to the investigation of RTT, which allows for direct manipulation of selected system parameters and testing of specific hypotheses. Specifically, we present three reduced computational models, developed using an established framework, all of which successfuly simulate respiratory outputs across eupneic and vagotomized conditions. All three models show that loss of inhibition to the Kölliker-Fuse nucleus reproduces the key respiratory alterations associated with RTT and, as suggested experimentally, that effects of 5-HT$_{1A}$ agonists on the respiratory neural circuit suffice to alleviate this respiratory pathology. Each of the models makes distinct predictions regarding the neuronal populations and interactions underlying these effects, suggesting natural directions for future experimental testing.

Key points:

- Reduced computational models are used to test effects of loss of inhibition to the Kölliker-Fuse nucleus (KFn).
- Three reduced computational models that simulate eupneic and vagotomized respiratory rhythms are considered.
- All models exhibit the emergence of respiratory perturbations associated with Rett syndrome as inhibition to the KFn is diminished.
- Simulations suggest that application of 5-HT$_{1A}$ agonists can mitigate the respiratory pathology.
- The three models can be distinguished and tested based on their predictions about connections and dynamics within the respiratory circuit and about effects of perturbations on certain respiratory neuron populations.

Keywords: breathing, Rett syndrome, Kölliker-Fuse nucleus, inhibition, serotonin, computational model

Acknowledgements: This work was partially supported by the US NSF awards DMS 1312508 (JR, SW) and 1612913 (JR) and by the National Center for Complementary and Integrative Health (NCCIH), NIH award R01AT008632 (AA).

1 Introduction

Rett syndrome (RTT) is a developmental disorder that is caused by mutations in the X-linked gene MECP2. Most RTT patients are young females; males with RTT typically do not survive the first years of life, although there are rare cases where affected males survive infancy. The disorder is responsible for a variety of symptoms, including neurocognitive impairment and pyramidal and extrapyramidal dysfunction. One of the most dangerous and disruptive symptoms of RTT is dysfunctional autonomic regulation of breathing, which is characterized by frequent and random apneas, periodic breathing (alternating bouts of rapid and low frequency breathing), and breath holds. Many instances of sudden death of children with RTT are a result of respiratory distress [77].

The MECP2 gene encodes the methyl-CpG binding protein 2 (MeCP2), a transcriptional regulator that plays a role in modulating the expression of a variety of neurotransmitters, neuromodulators, receptors, and neurotrophic factors. There has been a wealth of research using MECP2 knockout mice (KO mice) to characterize RTT respiratory dysfunction [70], to examine physiological consequences of MeCP2 deficiency, and to investigate possible clinical approaches to address associated concerns. Among the many neurotransmitters, neuromodulators, and neurotrophins found to be deficient in KO mice are GABA [16], norepinephrine [74], serotonin [74], and BDNF [36]. Furthermore, a variety of studies have found that acute and/or systematic application of various deficient neurotransmitters or selective receptor agonists can successfully rescue normal respiratory function to various degrees [74, 36, 3, 40, 4, 2, 38]. Of particular interest are 5-HT_{1A} agonists, which are currently being clinically tested for the specific indication of correcting breathing abnormalities in RTT [1].

Decades of research has established that the respiratory central pattern generator (rCPG) includes rhythmically interacting populations of inhibitory and excitatory neurons in the ventral respiratory column (VRC) in the medulla. Neurons within the VRC that activate at similar phases within the respiratory cycle tend to be spatially co-localized. Inspiratory and expiratory neurons are predominantly concentrated in the pre-Bötzinger (pre-BötC) and Bötzinger (BötC) complexes, respectively, although this compartmentalization is not precise [41, 56]. Descending projections from the VRC target premotor neurons in the rostral and caudal ventral respiratory groups (rVRG and cVRG) [67]. The rCPG circuits are subject to tonic and phasic drives from a variety of sources, including: (i) chemoreception mediated through the retrotrapezoid nucleus/parafacial respiratory group (RTN/pFRG) and caudal raphe; (ii) mechanoreceptive feedback from pulmonary stretch receptors and chemoreceptive input from carotid bodies mediated through the nucleus solitarus (NTS); and (iii) input

from various regions of the pons, perhaps most significantly the lateral parabrachial complex, including the Kölliker-Fuse nucleus (KFn) [39, 24, 67]. In normal breathing (or eupnea), afferent feedback contributes to regulating the transition between inspiration and expiration [39]. However, it has become clear that the pons (particulary the KF) also plays a major role in gating this transition, capable of acting in the absence of afferent feedback to help maintain a normal rhythm [23, 24]. It is clear that RTT involves imbalances in this complex network of interacting populations. Recent research suggests that a major cause of RTT respiratory arrhythmia is dysfunction in the interaction between NTS-mediated afferent feedback and pontine activity, causing overexcitability of KF neurons and dysregulation of the inspiratory off-switch (IOS). This dysfunctional interaction is hypothesized to result from deficiency in GABAergic and/or serotonin-mediated inhibition [70, 24, 2, 5].

There is a long tradition of using computational techniques to build models of this complex system, develop intuition about how it functions, and test hypotheses about the generation of respiratory rhythms [41, 50]. These models exist in many forms, from large scale models [62] to reduced population activity-based models [60], and have been designed to focus on a variety of specific aspects of respiratory function, including breathing following brainstem transections [66], active expiration [59, 51], and interacting pontine and afferent regulation of the breathing cycle [48]. Until now, however, there has not been a model designed to investigate RTT respiratory arrhythmia. In this work, we present three such models, using a reduced, population activity-based framework that allows us to identify the mechanisms underyling altered dynamics resulting from changes based on experimental results from KO mice. The models presented here were designed to examine the hypothesis that reduction or elimination of inhibition from medullary and pontine respiratory populations to the KF nucleus can result in the onset of RTT-like respiratory arrhythmia [5]. A variety of other well-characterized respiratory patterns are explored, in order to validate these models and thus establish their suitability for examination of simulated RTT conditions. Finally, the models are used to explore a mechanistic rationale for experimental findings using 5-HT_{1A} agonists to treat RTT respiratory dysfunction [3, 4, 2]. Based on these results, the models considered yield predictions related to the network dynamics underlying the emergence and potential suppression of RTT respiratory dysfunction, particularly spontaneous apneas. These predictions include some non-intuitive mechanistic insights and suggest some new directions for experimental investigation.

2 Methods

We developed, simulated, and analyzed three reduced respiratory models. Each model was considered in the following regimes: eupnea, Rett syndrome (RTT), and RTT with 5-HT_{1A} agonist application, all in intact and in vagotomized cases.

2.1 Model structure

One of the reduced models contains three distinct respiratory neuronal populations, and we refer to it as the *three population (3p) model*. The other two models contain four distinct respiratory neuronal populations each and have identical structure but different parameter tunings; we refer to these as the *four population escape (4p-e) model* and the *four population release (4p-r) models*. These names derive from the mechanism by which apnea is terminated in RTT simulations; details are discussed below. The general structure of the models is inspired by the models used in several earlier respiratory modeling studies [60, 59, 51]. The equations in this paper are based on one of these [59], except that rather than incorporating instantaneous synapses, we use the time-dependent synaptic variable dynamics from an earlier work [20]. Schematic diagrams illustrating the components of these models appear in Figure 1. Neuronal populations are considered to be synchronized in terms of transitions between active spiking and silent phases, although not in terms of precise spike times, and are thus effectively represented by single non-spiking neuron equations. The potential of each single neuron represents the average membrane potential of the corresponding population. The models that we consider reduce the four-neuron medullary respiratory kernel utilized in the previous studies into two neurons: a pre-Bötzinger Complex (pre-BötC) neuron and a Bötzinger Complex (BötC) neuron. The pre-BötC component is used to represent inspiratory pre-motor output, while the BötC population is used to represent the cumulative expiratory pre-motor output. Thus, for the sake of simplicity, "I population", "inspiratory population", and "pre-BötC" are used interchangeably, as are "E population", "expiratory population", and "BötC".

The medullary kernel is modulated by a variety of inputs. As in previous studies [60, 59, 51], some of these inputs are represented as simple tonic drives stemming from tonic populations in the medulla and the pons. The models contain a simplified representation of pulmonary stretch receptor (PSR) feedback (as mediated through the NTS) derived from the output of the I population, in contrast to explicit representations of the lungs and NTS pump cells [51]. Additionally, a novel feature in the two 4p models is the inclusion of two phasic pontine populations: an inspiratory-modulating parabrachial population (PB-I) and an expiratory-modulating Kölliker-Fuse (KF) population (KF-

E). Alternatively, in the 3p model, we include only one phasic pontine population, representing the KF-E. The connections involving the pontine populations are based on a previous large scale model [62] and experimental evidence of intrapontine inhibition [17, 54, 53, 24], including studies supporting the idea that KF activity induces inhibitory effects (see [24] and the references therein).

In all models, vagotomy is simulated by deactivating all pathways mediated by the NTS. The models do not mathematically represent peripheral chemoreceptors. RTT is simulated by weakening GABAergic inhibition of the KF-E population. Recent findings have demonstrated that blocking GABAergic inhibition in the KF of wild-type rats is sufficient to create an RTT-like respiratory pattern [5]. Thus, in RTT simulations, we only weaken inhibitory projections to the KF from populations proven to release GABA, namely the NTS, BötC, and PB-I [27, 28, 26]. We also explore the use of a 5-HT_{1A} agonist as a treatment for RTT respiratory dysfunction [40, 4, 2]. To simulate the application of a 5-HT_{1A} agonist, we strengthened inhibitory connections within the medullary kernel and we activated 5-HT_{1A}-sensitive potassium channels in all populations (detailed in the equations below), based on previous modeling work [64].

All model neurons include an intrinsic burst generation capability within some parameter regime based on the activity of the persistent sodium currrent (I_{NaP}) [15, 21, 37, 20] (see Table 1 below), but in practice most are not tuned to the intrinsic bursting regime and their outputs are largely influenced by connections within the networks shown in Figure 1 [66].

2.2 Model specification

In describing the 4p models, we use subscripts $i \in \{$ *pbc,bc,kf-e,pb-i* $\}$ to represent the I (pre-BötC), E (BötC), KF-E, and PB-I populations, respectively. In the equations for the 3p model, we use $i \in \{$ *pbc,bc,kf-e* $\}$ to represent the I (pre-BötC), E (BötC), and KF-E populations, respectively. The average membrane potential of each population in all models evolves according to the voltage ordinary differential equation (ODE)

$$\frac{dV_i}{dt} = (-I_{NaP_i} - I_{K_i} - I_{L_i} - I_{ton_i} - I_{syn-I_i} - I_{syn-E_i} - I_{KS_i} - \Gamma_i)/C. \tag{2.1}$$

In equation (2.1), I_{NaP_i} represents the current through persistent sodium channels, I_{K_i} is the potassium delayed rectifier current, I_{L_i} is the leakage current, I_{ton_i} is cumulative current from all sources of tonic drive, I_{syn-I_i} and I_{syn-E_i} are currents from inhibitory and excitatory synaptic channels, respectively, I_{KS_i} is current through 5-HT_{1A}-sensitive potassium channels, and Γ_i is a noise term. The transmembrane currents are given by

the following equations:

$$
\begin{aligned}
&I_{NaP_i} = g_{NaP_i} \cdot m_{NaP,\infty}(V_i) \cdot h_i \cdot (V_i - E_{Na}),\\
&I_{K_i} = g_K \cdot m_{K,\infty}(V_i)^4 \cdot (V_i - E_K),\\
&I_{L_i} = g_L \cdot (V_i - E_L),\\
&I_{ton_i} = c_i \cdot (V_i - E_{syn-E}),\\
&I_{syn-I_i} = g_{syn-I} \cdot (V_i - E_{syn-I}) \cdot (1 + k_s \cdot k_{\alpha 3_i}) \cdot \textstyle\sum_{j=1;j\neq i}^{4} b_{j,i} \cdot s_{j,i},\\
&I_{syn-E_i} = g_{syn-E} \cdot (V_i - E_{syn-E}) \cdot \textstyle\sum_{j=1;j\neq i}^{4} a_{j,i} \cdot s_{j,i},\\
&I_{KS_i} = g_{KS_i} \cdot m_{KS}([S]) \cdot (V_i - E_K),
\end{aligned}
\tag{2.2}
$$

while Γ_i is a normal random variable with zero mean and standard deviation γ_i.

Inactivation of persistent sodium channels (h_i) and the time course of the synaptic conductance from cell j to cell i ($s_{j,i}$) are modeled using the following ODEs:

$$
\begin{aligned}
&\tfrac{dh_i}{dt} = (h_{\infty_i}(V_i) - h_i)/\tau_{h_i}(V_i),\\
&\tfrac{ds_{j,i}}{dt} = \alpha \cdot (1 - s_{j,i}) \cdot s_{\infty_i}(V_j) - \beta_{j,i} \cdot s_{j,i},
\end{aligned}
\tag{2.3}
$$

which are standard in the Hodgkin-Huxley framework.

Voltage-dependent activation functions and time constants in equations (2.2), (2.3) are described by the following functions:

$$
\begin{aligned}
&h_{\infty_i}(V_i) = 1/(1 + \exp[(V_i - \theta_{h_i})/\sigma_h]),\\
&s_{\infty_i}(V_i) = 1/(1 + \exp[(V_i - \theta_{syn_{j,i}})/\sigma_{syn_{j,i}}]),\\
&\tau_{h_i}(V_i) = \epsilon_i/(\cosh[(V_i - \theta_{\tau_i})/\sigma_{h_i}/2]),\\
&m_{NaP,\infty}(V_i) = 1/(1 + \exp[(V_i - \theta_{m_{NaP}})/\sigma_{m_{NaP}}]),\\
&m_{K,\infty}(V_i) = 1/(1 + \exp[(V_i - \theta_{m_K})/\sigma_{m_K}]).
\end{aligned}
\tag{2.4}
$$

Note that in the $s_\infty(V)$ equation in (2.4), the subscript j denotes the source or pre-synaptic population, the subscript i the post-synaptic target.

Application of a 5-HT$_{1A}$ agonist is simulated with two changes in the model: increased inhibitory strength and activation of I_{KS} channels [40]. The first perturbation is implemented by making the factor k_s in the I_{syn-I_i} equation in system (2.2) nonzero, and the second depends on the following function that appears in system (2.2), where $[S]$ is the agonist concentration and $[S]_t$ is a saturation threshold [64]:

$$
m_{KS}([S]) = 1/(1 + \exp[([S]_t - [S])/2]) \tag{2.5}
$$

Note that I_{KS} has a straightforward hyperpolarizing effect and hence could also represent contributions from other sources of hyperpolarization with similar reversal potentials (cf. [44, 58]).

The tonic drive term, I_{ton_i}, includes a coefficient c_i reflecting the inclusion of two sources, the pons and the medulla, the contributions of which are represented by pd_i and med_i respectively:

$$c_i = pd_i + med_i. \tag{2.6}$$

Table 1 describes the intrinsic behavior of the neurons in all three models, both with and without the tonic excitatory connections (green triangles in Figure 1). Knowing how each model neuron behaves in the absence of phasic inuts from other neurons can provide important context for the model dynamics and predictions. Table 2 lists the values of parameters that are not population-specific and are shared by all models. Tables 3 and 4 present the values of additional non-synaptic parameters and synaptic parameters, respectively, in the 3p model; Tables 5 and 6 display the values of these non-synaptic and synaptic parameters, respectively, in the 4p-r model; and Tables 7 and 8 include the values of these non-synaptic and synaptic parameters in the 4p-e model. Parameter values for all models were derived by starting from previous models [59, 64, 51] and introducing perturbations to achieve appropriate dynamics. In the 3p model, the KF-E unit could initiate the inspiratory off-switch in the vagotomized state [55, 68]. In the 4p models, the introduction of the PB-I population resulted in an intact source of inhibition to the KF-E population during the inspiratory phase of the vagotomized regime. Therefore, in the 4p models, KF-E could not directly initiate the I-E phase transition during vagotomy, as occurs in the 3p model, but nonetheless contributed to expiration in the vagotomized state [53].

Apneas in RTT simulations are terminated by noise-induced activation of the I unit in the 4p-e model and by noise-induced deactivation of the KF-E unit in the 4p-r model. This distinction in dynamics arises from several key parameter differences between the models. Specifically, compared to the 4p-e model, (1) the E unit inhibits the I unit more strongly in 4p-r, providing a stronger suppression of I activation (see parameter $b_{bc,pbc}$), (2) the E unit more strongly inhibits the KF-E in 4p-r, so that even with some loss of inhibition the KF-E unit is more susceptible to deactivation by noise (see parameter $b_{bc,kf-e}$), and (3) tonic drive to the KF-E is reduced in 4p-r, which also enhances the likelihood of KF-E deactivation (see parameters pd_{kf-e} and med_{kf-e}).

Simulations were performed using an adaptive Runge-Kutta algorithm in the freely available XPPAUT software package [25], sometimes with a MATLAB (versions 9.0-9.5) interface for iterations over parameter values. All simulations were performed on a typical PC laptop (HP ProBook 450 G1). Most simulations were completed in under an hour. Simulations for Figures 5 and 9 were completed overnight.

2.3 Phase plane analysis

Output patterns were analyzed by projecting network solutions, or trajectories, to phase planes defined by the voltage and persistent sodium inactivation variables for individual neurons and visualizing these together with relevant nullclines. For a system of two differential equations, in the phase plane formed by plotting one dependent variable against the other, each variable's nullcline is the collection of points for which the right-hand side of its differential equation equals 0; typically these form curves. Nullclines can help to explain the dynamic mechanisms underlying an observed output pattern. In our models, over at least some parameter range, each V-nullcline consists of a cubic-shaped curve in the (V, h) phase plane, with an attracting branch at low voltages corresponding to an inactive or silent phase, an unstable middle branch, and an attracting branch at elevated voltages corresponding to an active phase; if V represents average voltage across a neuronal population, then individual neurons within the population would be spiking in the active phase. When projected to the phase plane of each neuron, a trajectory mostly stays near the lower (silent) or upper (active) branch of each neuron's V-nullcline, with occasional rapid switches between branches. The concepts of *escape* and *release* are useful for considering how these switches can occur [75, 65, 20].

The simple example shown in Figure 2 illustrates the concepts of escape and release in a network of two neurons coupled by mutual synaptic inhibition. The neurons in the example network are mathematically similar to the model pre-BötC and BötC neurons, but their parameters are tuned differently (and unequal to each other) for illustrative purposes. The voltage time courses for the coupled network exhibit transitions in which the two neurons switch their active and silent roles (Fig. 2A). Importantly, the position of the V-nullcline for a neuron in a synaptically coupled network depends on the synaptic inhibition it receives from other neurons (based on the I_{syn} terms in equation (2.1)). Fig. 2B shows example V-nullclines for cell 1. The voltage nullcline corresponding to full inhibition from cell 2 to cell 1 (maximal $s_{2,1}$) is plotted in solid red, while the voltage nullcline corresponding to no inhibition to cell 1 (i.e., when cell 2 is inactive) is plotted in the dashed red curve. The cyan curve shows the nullcline for the inactivation variable h for cell 1, based on equation (2.3). Fixed points of the system, for a fixed inhibition level, occur at the intersection of the voltage nullcline corresponding to that inhibition level and the inactivation nullcine. The black cycle is the trajectory from Fig. 2A projected to the (V_1, h_1) phase plane. The vertical dotted black line shows the synaptic threshold for synaptic inhibition from cell 1 to cell 2 and from cell 2 to cell 1 (i.e., in this parameter tuning, $\theta_{syn_{1,2}} = \theta_{syn_{2,1}}$; see system (2.4)) When cell 1 is inhibited by cell 2, the projected trajectory evolves slowly up the left

branch of the full-inhibition V_1-nullcline. At the point marked with a black square, V_1 reaches the left local extremum, or knee, of its nullcline, where the silent branch ends. The trajectory then undergoes a rapid excursion to the right, in the direction of increasing voltage, crossing the threshold for synaptically inhibiting cell 2. This type of transition, driven by the voltage of the silent cell, is called an *escape*. The inhibitory conductance $s_{1,2}$ becomes large and this change adjusts the V-nullcline for cell 2, such that cell 2 transitions to the silent phase and $s_{2,1}$ drops close to 0. Thus, the projected trajectory in the (V_1, h_1) phase plane approaches the dashed V_1-nullcline corresponding to the uncoupled dynamics of cell 1 near $V_1 = -10mV$. The trajectory evolves slowly down the right branch of this no-inhibition V_1-nullcline in the (V_1, h_1) phase plane. At the point marked with a gray circle, it reaches the right knee of the V_1-nullcline, where the active nullcline branch ends in another nullcline knee. The trajectory then undergoes another rapid transition, in the direction of decreasing voltage, which brings it through the synaptic threshold and causes $s_{1,2}$ to approach 0. This transition driven by the active cell, called *release*, allows cell 2 to activate.

Fig. 2C displays the nullclines and projected trajectory for cell 2. Analogously to cell 1, between rapid jumps in voltage, the trajectory projected to the phase plane for cell 2 evolves along branches of the V_2-nullcline, corresponding to the level of inhibition it is receiving. When cell 2 is active, however, it cannot reach the right knee of the uninhibited V_2-nullcline (indeed, parameters are tuned such that this nullcline is monotonic, without knees; see dashed nullcline in Fig. 2C). Thus, cell 2 cannot initiate a transition by release. Similarly, when cell 2 is silent, it cannot reach the left knee of the inhibited V_2-nullcline due to the presence of a fixed point, where the V_2- and h_2-nullclines intersect (near the grey circle in Fig. 2C). Thus, cell 2 cannot initiate a transition by escape. In the projection of the trajectory from Fig. 2A, which is shown in blue, cell 2 jumps to high voltage and thus becomes active only when it is released by cell 1 (grey circle) and jumps down to low voltage and thus becomes inactive only when cell 1 escapes (black square), as described above.

3 Results

The purpose of this study was to use computational modeling to test the hypotheses that (1) the variable, apneic breathing patterns observed in Rett syndrome can arise from loss of inhibition to respiratory neurons in the Kölliker-Fuse nucleus (KF-E unit in the model), and (2) the restoration of eupnea-like breathing patterns by serotonergic (5-HT$_{1A}$) agonist application in Rett syndrome can arise from these agonists' influence on 5-HT-activated potassium channels (see *Methods*). To achieve these aims, we

utilized minimalistic reduced computational models that allow for clear elucidation of mechanisms underlying simulation outcomes and hence direct mapping of results to mechanistic biological predictions. In this modeling framework, differential equations for a single neuron or unit lacking spiking currents were used as a proxy for the dynamics of each biological neuronal population, justified by the assumption that each relevant population exhibits relatively synchronized transitions between low and high activity states, but with asynchronous spiking that would result in a net averaging out of spikes over the population (see *Methods*).

Two different base models were developed: one model comprised three potentially rhythmic respiratory neuron populations, including KF-E, and hence was dubbed the 3p model (Fig. 1A); the other model supplemented these three populations with a second pontine population from outside of the KF, which we denote with the general label of parabrachial (PB-I), and thus was called the 4p model (Fig. 1B). Two 4p model variants (4p-e and 4p-r) were considered, distinguished by their parameter tunings (see *Methods*) but not by their structural features. In each model, the dynamics of the inspiratory pre-BötC unit and the expiratory Bötzinger complex (BötC) unit depended on a persistent sodium current that allowed rhythmicity of that unit for certain fixed input levels [66, 7], although similar dynamics would arise from other currents that enhance excitability in the silent phase and feature slow negative feedback [34]. Each of the 3p, 4p-e, and 4p-r models was tuned to produce experimentally observed patterns under several conditions, as described below, and then tested under simulated Rett syndrome, with and without 5-HT_{1A} agonist application. Differences between the 4p-e and 4p-r models have minimal effects on eupneic and vagotomized dynamics and will be discussed in the context of RTT, since simulated RTT unmasks these differences.

3.1 Intact models produce eupneic breathing patterns

Each of the three models, given its baseline parameter tuning and arbitrary initial conditions, settled into an activity pattern corresponding to a eupneic respiratory rhythm (Fig. 3A,D). Although a specific baseline parameter set was chosen for each model, this pattern was robust to reasonable parameter variations. In all cases, this rhythm consisted of a periodic alternation (at frequencies appropriate for mouse or rat) of phases of elevated inspiratory activity with phases of elevated expiratory activity, such that the expiratory activity duration was about twice the inspiratory activity duration (3p: $T_i = 328ms, T_e = 514ms$; 4p-r: $T_i = 355ms, T_e = 673ms$; 4p-e: $T_i = 365ms, T_e = 601ms$). KF-E activity was suppressed in these patterns, while the additional PB-I unit in the 4p cases exhibited moderate activity that was approxi-

mately tonic but with small surges that did not contribute to rhythm generation, which occurred in response to its inputs from the inspiratory pre-BötC unit (Fig. 1B).

We used nullclines to understand the dynamic mechanisms underlying the models' eupneic rhythmicity, which in our simple modeling framework depended on the persistent sodium current, I_{NaP}. Since the I_{NaP} inactivation variable h evolves much more slowly than voltage, the voltages of the pre-BötC and BötC units would rapidly equilibrate to quasi-steady states, with subsequent voltage dynamics slaved to h except during rapid switches between inspiration and expiration. Thus, the model trajectory projected to the phase space variables of one unit, such as (V_{pbc}, h_{pbc}) for the pre-BötC unit or (V_{bc}, h_{bc}) for the BötC unit, would generally lie on the voltage nullcline, or curve of zero voltage time derivative, of that unit except during the fast switches. Which nullcline was selected at any time corresponded to the level of inputs received by the unit at that time (see *Methods*).

In the intact 3p model (Fig. 3A-C), although the BötC unit could oscillate in the absence of inhibition, it received enough inhibition during inspiration to prevent it from activating (grey circle, Fig. 3C). The switch from inspiration to expiration occurred when the voltage of the active pre-BötC unit hyperpolarized to a level close to the synaptic threshold (black dashed line, Fig. 3B), corresponding to adaptation after an extended active period (grey circle, Fig. 3B). The resulting loss of inhibition allowed the voltage nullcline of the BötC unit to settle to a lower position (dash-dotted red curve, Fig. 3C), such that the unit could transition to the active phase. After this activation, the BötC unit inhibited the KF-E unit, causing KF-E to remain inactive, and provided just enough inhibition to prevent the activation of the pre-BötC unit (black square, Fig. 3B). The switch from expiration to inspiration thus relied upon a small degree of adaptation of the active BötC unit, which lowered the voltage nullcline of the pre-BötC unit enough to allow it to activate (Fig. 3B, inset), although much less adaptation was needed than during the switch from inspiration to expiration. Finally, during inspiration, feedback signals through the vagal pathway via the NTS inhibited KF-E, maintaining its inactivity and its lack of contribution to the eupneic rhythm.

The 4p-e and 4p-r models produced almost identical eupneic rhythms to each other. In these activity patterns, the switch from expiration to inspiration was similar to that in the 3p model (black squares, Fig. 3E,F; inset, Fig. 3E), as was the suppression of the KF-E unit during both expiration and inspiration. Unlike the 3p case, however, the switch from inspiration to expiration occurred without adaptation when the suppressed BötC unit, despite being fully inhibited by the active pre-BötC unit, was able to reach the fold of its voltage nullcline and enter the active phase by escape (grey circles, Fig. 3E,F; see *Methods* for discussion of transitions by escape); that is, although the BötC

unit was not intrinsically rhythmic without input, inhibition yielded sufficient deinactivation of persistent sodium to allow it to eventually activate, highlighting a possible role for slow inward currents even in neurons lacking intrinsic rhythmicity (related to post-inhibitory rebound, cf. [30, 20]). The tuning of parameters to allow this escape was necessary for the model to produce both eupneic outputs with KF-E suppression under baseline conditions and appropriate rhythmic outputs under vagotomy despite the loss of vagal input, without requiring an intrinsically rhythmic KF population (see next section).

3.2 Models produce slower breathing patterns with prolonged expiration under simulated vagotomy

Various experimental models study respiratory rhythm generation after vagus nerve transection. Despite the loss of vagal input to respiratory neural populations, this manipulation yields respiratory rhythms maintaining the basic inspiratory-expiratory phase alternation, but with a longer period and with increased ratio of expiratory duration to inspiratory duration [52, 18, 23]. Our model networks all reproduced these features (Fig. 4A,E). In all cases, the KF-E unit in the model became rhythmic, activating during expiration and falling inactive during inspiration (green traces, Fig. 4A,E) In the 4p models, KF-E activity alternated with PB-I activity, such that the PB-I unit was active during inspiration and inactive during expiration (hence the labels E for the KF-E unit and I for the PB-I unit). Different dynamic mechanisms gave rise to the vagotomized rhythms in the 3p and 4p models, however.

In the 3p case (Fig. 4A-D), the loss of vagal input rendered the BötC unit unable to activate even after the adaptation of pre-BötC activity (grey circles, Fig. 4B,C). In the absence of vagal inhibitory feedback signals, however, the KF-E unit was able to transition autonomously into the active phase (grey circle, Fig. 4D). Once this activation occurred, the excitation from the KF-E recruited BötC activity and helped sustain a prolonged expiratory phase. The inhibition from the BötC unit to the KF-E (Fig. 1) did not interfere with this maintained expiration, since the voltage nullcline of the KF-E unit, even in the presence of this inhibition, featured an extended active phase branch (4D, dashed V-nullcline). Once the KF-E unit finally reached the end of this branch, it became inactive again, removing a source of excitation to the BötC unit and causing the BötC unit to become inactive, thereby releasing the pre-BötC unit and allowing inspiration to commence (black squares, Fig. 4B-D).

The 4p models were specifically designed to explore the alternative hypothesis that the KF-E population, even in the absence of vagal feedback inhibition, could not au-

tonomously generate rhythmicity. This constraint is manifested in the existence of a stable fixed point on the left branch of the KF-E unit's voltage nullcline in the absence of input in the 4p case (grey circle, Fig. 4H). In the 4p models, parameters were tuned such that in the absence of vagal feedback excitation, the BötC unit was still able to transition to the active phase once the pre-BötC unit adapted sufficiently (grey circles, Fig. 4F,G; see also inset of Fig. 4E, which illustrates that BötC unit activation precedes KF-E activation) Note that the BötC activation here does require that it receives a sufficiently strong tonic drive, some of which could come from pontine sources [6]. Without KF-E, our model would still produce a rhythm but with a greatly shortened E phase (analogous to the 2-phase rhythm seen experimentally with pontine transection [66, 61]), whereas the loss of all pontine drive to the BötC unit yielded apneusis. The BötC unit's transition to the active phase was delayed relative to the eupneic case, resulting in an increased inspiratory duration in vagotomized rhythms relative to eupneic rhythms, which stands as a prediction of the 4p models. In this case, the loss of pre-BötC activity removed the drive to the PB-I unit and hence its inhibition of the KF-E unit as well. This loss of inhibition lowered the KF-E unit's voltage nullcline relative to its position with inhibition from the PB-I and BötC present (Fig. 4H, dashed V-nullcline) and subsequently allowed the KF-E unit to activate fully, despite the inhibition it received from the BötC unit. Once it was active, the excitation from the KF-E to the BötC pinned the BötC in the active phase and correspondingly prolonged expiration, and enhanced the adaptation of the BötC unit, until the KF-E activity adapted and the KF-E unit became inactive again (black square, Fig. 4H). Finally, the loss of excitation from KF-E to BötC, following the inactivation of KF-E, caused the BötC unit to become inactive (Fig. 4G) and released the pre-BötC unit to activate and initiate the next phase of inspiration (Fig. 4F), as in the 3p model. Thus, this model does include a contribution of KF-E to the transition from expiration to inspiration.

Several predictions come out of the differences between the models, their dynamic mechanisms, and their parameter tunings in the vagotomized regime. First, in the 3p case, blockade of KF-E activity should prevent the termination of inspiration, whereas in the 4p cases, expiratory interruptions of inspiration would still be possible without KF-E participation, although they might be brief. Correspondingly, a surge in KF-E activity would be predicted to precede activation of BötC in the 3p but not the 4p cases (Fig. 4A and E: compare insets). Moreover, the inspiratory off-switch would be more robust to the application of hyperpolarizing current to the BötC in the 3p case than in the 4p cases. Second, as we have already noted, the 4p models predict that vagotomization will increase the duration of inspiration, whereas the 3p model

does not. Figure 9 provides a comparison of inspiratory, expiratory, and total cycle durations across models and conditions and clearly makes the comparison of the intact and vagotomized cases (additional scenarios shown in the figure will be discussed below). Third, the 3p model predicts, somewhat counterintuitively, that under vagotomy the KF-E is subject to stronger inhibitory inputs during expiration than during inspiration, whereas the 4p models predict the opposite (Fig. 4D and H: compare relative positions of solid and dashed V-nullclines). Fourth, due to the differing influences of the KF-E unit on the voltage nullcline of the BötC unit while both are active, the 3p model predicts that expiration can continue slightly beyond the inactivation of the KF-E, whereas any such extension would be absent or extremely limited in the 4p models.

3.3 Models produce activity patterns characteristic of RTT under block of inhibition to the KF-E

Experimental studies have suggested that a loss of GABAergic inhibition to respiratory neurons within the KF-E may represent a key factor in the emergence of the altered breathing patterns associated with RTT and the MECP2 knockout mouse model [5, 3, 46]. Our computational models are designed to test the viability of this idea. To do so, we gradually reduced the strength of various inhibitory connections targeting the KF-E unit in the model (Fig. 1, connections marked with R) and observed the resulting model dynamics. In all cases, we reduced the strength of the direct inhibitory projection from the BötC unit to the KF-E. In our simulations of RTT conditions within an intact system, we also reduced the strength of the connection representing inhibition from the NTS to the KF-E; this connection was absent in our simulations of RTT conditions in a vagotomized state. Finally, in the 4p models, we also reduced the intrapontine inhibition from the PB-I to the KF-E, although this inhibition was not reduced all the way to zero, reflecting the likely contribution of glycinergic inhibition within the pons. The strength of this inhibitory connection was reduced by up to 50% in the 4p-e model and 30% in the 4p-r model. With more severe reductions, the BötC neurons in both 4p models lost the ability to escape in the vagotomized regime without excitatory drive from the KF-E. As the 4p models were designed to explore the hypothesis that the BötC neuron is able to escape without the KF-E, we selected the reductions accordingly, informed by knowledge of the presence of multiple inhibitory transmitters in the pons [53, 24]. In all cases in which multiple connections were altered, parameter changes were made proportionately using a scaling factor; if we let $\alpha \in [0, 1]$ denote the fraction of total inhibition present, then each affected connection strength was set to $p_{min} + \alpha(p_{max} - p_{min})$, where p_{min}, p_{max} denote the minimum and maximum values, respectively, for that

strength. All three models exhibited an increase in expiratory duration and variability as inhibition was reduced, as detailed below; furthermore, consistent with experiments [70, 5], glutamate injection to the KF-E, simulated by turning on a tonic excitatory current with reversal potential $0mV$, prolonged expiration, with a stronger effect in RTT than in control conditions, in all of the models (data not shown).

The 3p and 4p-r models in the intact case showed qualitatively similar behaviors as inhibition was reduced (Fig. 5A,B). After an initial interval of insensitivity to changes in inhibition, an interval of inhibition levels occurred in which usual cycles were occasionally interrupted by apneic cycles (i.e., cycles with prolonged expiration), leading to an increase in average period and in variability. Below this inhibition interval (with approximately 20-50 % of inhibition remaining for 3p and 10-30 % of inhibition intact for 4p-r), regular rhythmicity re-emerged, but with prolonged expiratory duration . Finally, for inhibition below these levels, apneas became even longer and more irregular, with progressively more variability and increased mean apnea duration as inhibition was progressively decreased. In the 3p case, once inhibition dropped below $\sim$10% of normal, rhythmicity was lost, whereas in the 4p-r case, rhythmicity was maintained all the way down to $\alpha = 0$ (Fig. 5A,B).

The 4p-e model also yielded increased variability and apnea duration, leading to corresponding changes in period, as inhibition to the KF-E was gradually diminished, with a qualitatively similar progression to the 4p-r and 3p cases (Fig. 5C). The three abnormal regimes in the 4p-e model are illustrated in Fig. 5D (green circle: occasional apneas; yellow square: regular apneas; red triangle: variable duration, generally prolonged apneas). The 4p-e case featured more of a gradual transition from the regime in which all expiratory cycles were prolonged (yellow square) to the highly variable regime (red triangle) than the other models, in that it featured some variability in period throughout the entire corresponding range of inhibition levels.

The activity patterns of the 3p and 4p-r models were less similar under our simulations of the gradual loss of inhibition to the KF-E in the vagotomized case. In the 3p model, because the KF-E activated to initiate expiration and only became inhibited after expiration was underway, the loss of up to 80% of inhibition had almost no effect on network outputs (Fig. 5E). From inhibition levels at 20% of baseline down to 10% of baseline where rhythmicity was lost, significant apneas with extensive variability could finally emerge, due to prolonged KF-E activation. Like the 3p model, the vagotomized 4p-r model also showed a loss of the intermediate regime of variable expiratory durations after initial apnea onset (compare Fig. 5 A-B versus E-F). In the 4p-r case, however, variability appeared with a much larger fraction of inhibition still remaining and became progressively more extreme, with corresponding increases in mean respi-

ratory cycle period. Finally, the vagtomized 4p-e model did not show much variability until inhibition had dropped by about 50%, after which an abrupt increase in variability and average period occurred, which were maintained down to complete inhibition blockade (Fig. 5G). Once the initial onset of variability had arisen, the progression for the vagtomized 4p-e model was quite similar to that for the intact 4p-e model (compare Fig. 5C vs. Fig. 5G).

We can partially explain the differences between the 4p-r and 4p-e models by consideration of model activity patterns in appropriate phase planes. In our simulations of severe RTT (i.e., sufficient reduction of inhibition to KF-E), the lessened inhibition of the KF-E yields a stable fixed point, corresponding to tonic activation of KF-E (black circle, Fig. 6) and suppression or inactivity of the pre-BötC unit (yellow circle, Fig. 7). Because noise is included in the system, projections of trajectories to these phase planes do not approach the fixed point asymptotically but rather approach a small neighborhood of this fixed point. Orbits in this neighborhood exhibit small-amplitude oscillations because the fixed point is a stable spiral point. Noise produces an effective voltage threshold, such that if, on a particular oscillation cycle, the projection of the orbit to the KF-E phase plane drops below the KF-E voltage associated with this threshold, then KF-E activation terminates, inducing a corresponding loss of BötC activation. On the other hand, if the projection of the orbit to the pre-BötC phase plane crosses above the pre-BötC voltage associated with the threshold, then the pre-BötC unit can activate.

In the 4p-r model, parameters are tuned such that the KF-E active phase right branch fixed point lies near the right knee of its V-nullcline in the active phase, which strongly favors the former scenario of expiratory phase termination by KF-E and BötC deactivation (see Methods for full details of parameter differences between 4p-r and 4p-e models). This deactivation releases the pre-BötC unit from inhibition and thus allows it to activate, hence the name 4p-r, which refers to 4p with release. In the intact case, a significant reduction of inhibition to KF-E is needed before the stable fixed point and associated prolonged, variable expiratory phase duration can arise, as seen in Figure 5B. In the vagotomized case, noise can prolong KF-E activation even for relatively large inhibition levels, for which the fixed point is not stable but is close to a bifurcation that will stabilize it. As inhibition gradually decreases, the KF-E activation level becomes more elevated relative to the threshold for KF-E deactivation, such that deactivation becomes less likely and the magnitude and variability of apnea duration increase (Fig. 5F).

In the 4p-e model, parameters are tuned such that the fixed point for the pre-BötC unit under full inhibition lies near the left knee of its V-nullcline, which strongly favors

noise-induced activation, or escape, of the pre-BötC unit, hence the name 4p-e for 4p with escape (see Methods). This effect can arise fairly similarly in the intact and vagotomized cases. In the intact case, however, alterations to the basic rhythm can emerge with less reduction of inhibition to the KF-E because KF-E activation starts to occur on occasional cycles (Fig. 5D, green circle); in the vagotomized case, KF-E already activates on each cycle, so there is no opportunity for this transitional regime. Note that in the 4p-e model, during an extended apnea, some adaptation of the BötC unit occurs, yielding a corresponding mild reduction in inhibition to the pre-BötC unit. This change allows the fixed point for the pre-BötC unit to drift to slightly lower h_{pre-I} values, with a corresponding drift in the vertex of the spiraling trajectory observed in projection to the pre-BötC phase plane (Fig. 7) and in the effective voltage threshold for pre-BötC unit activation.

Finally, the mechanistic difference in the apnea termination mechanisms in the 4p-r and 4p-e models gives rise to some clear differences in the predictions they make about how the respiratory neural network will respond to perturbations in RTT conditions. In the 4p-r model, the initiating step in apnea termination is a fluctuation-induced loss of KF-E activation (Fig. 6), while in the 4p-e model, termination originates with the onset of pre-BötC activation (Fig. 7). Therefore, in the 4p-r model, the application of weak depolarizing stimulation to the KF-E unit, by preventing the loss of KF-E activation, yields sustained KF-E and BötC activity and prevents the termination of expiration (Fig. 8, upper left). Alternatively, the application of weak hyperpolarizing input to the pre-BötC unit has little effect on apnea properties in the 4p-r model, since this stimulation does not interfere with the loss of KF-E activation (Fig. 8, upper right). In contrast, in the 4p-e model, the application of weak depolarizing stimulation to the KF-E unit does not noticeably affect apnea termination, since this stimulation does not impact the ability of the pre-BötC unit to activate (Fig. 8, lower left). The application of weak hyperpolarizing input to the pre-BötC in the 4p-e model, however, will suppress pre-BötC activation and hence lead to sustained KF-E and BötC activation and expiration (Fig. 8, lower right).

3.4 Application of a 5-HT$_{1A}$ agonist in simulated RTT normalizes expiration

Our simulation results show that sufficient reduction of inhibition to the KF-E in simple respiratory neural models induces the prolonged expiration and increase in expiratory variability associated with breathing in RTT. Experimental work has suggested that loss of 5-HT$_{1A}$-mediated inhibition could induce respiratory cycle irregularity [22], that

application of 5-HT$_{1A}$ agonists improves cycle regularity even in wild-type mice [70], and that such agonist application could alleviate variability and prolonged expiration in RTT [40, 4, 2]. Hence, we next explored the effects of simulated 5-HT$_{1A}$ agonist application in our models. To represent this intervention, we strengthened inhibitory connections within the medullary kernel as well as the glycinergic component of the inhibition from the PB-I to the KF-E that was maintained in our simulated RTT conditions and, following previous computational modeling [64], we activated a 5-HT$_{1A}$-sensitive hyperpolarizing (e.g., potassium) current in all populations. Although the adjusted inhibition levels modified V-nullcline positions, the dominant effect of this modification occurred via the potassium channel adjustment. This change caused a significantly earlier, stronger adaptation of the BötC unit during expiration, shortening expiratory durations to near the levels associated with intact eupneic breathing in the moderate RTT case and toward the levels associated with vagotomized eupneic breathing in the severe RTT case (Fig. 9). For comparison, we also simulated 5-HT$_{1A}$ agonist application in the intact and vagotomized eupneic cases. Interestingly, in the 4p models, we observed a slight lengthening of inspiration in the intact case and a slight shortening of expiration in the vagotomized case, which reflects a stronger effect of 5-HT$_{1A}$-sensitive potassium channels on the BötC unit than on the pre-BötC unit and stands as a prediciton of our model tuning (Fig. 9).

4 Discussion

RTT leads to dysfunctional breathing that includes extended, variable apneas. Identifying the source of these breathing disruptions would be a key step in developing therapeutic interventions and would also provide insights about basic properties of respiratory rhythm generation and control. This study takes a novel step in the investigation of RTT: we have harnessed a reduced computational modeling framework, which allows direct manipulation of specific network components without confounds associated with experimental techniques, to perform simulations spanning multiple network configuration states and a clinical intervention. Our results demonstrate that loss of GABAergic inhibition to the KF nucleus could underlie the prolongation and variability of expiration in RTT, as suggested by recent experiments [3, 5], and that effects of 5-HT$_{1A}$ agonists on inhibitory interactions and membrane potentials in the respiratory neural circuit suffice to alleviate this respiratory pathology [40, 4, 2]. We obtained these results using not just one but three related but distinct models, each of which makes distinct predictions about which key pathways and interactions allow these effects to emerge (Fig. 1), providing natural targets for exploration in future experiments. Our

findings also make predictions that go beyond scenarios considered in previous experiments, specifically suggesting that respiratory outputs should show some resilience to the gradual reduction of inhibition to the KF, followed by a gradual enhancement of expiratory duration and variability (Fig. 5), all of these which can be tested in future experiments to evaluate how the loss of GABAergic inhibition to the KF contributes to the respiratory alterations observed in RTT.

Although our models are simplified, they are well grounded in experimental results and past literature. The medullary rhythm generation circuit within the model relies on mutually inhibitory synaptic connections between inspiratory and expiratory units. There is a long history of including such interactions in conceptual and computational models of respiratory neural circuitry (reviewed by Lindsey et al. [41]), with recent new insights underlining their importance (e.g., [51, 45, 32, 8, 11, 56]). An earlier large-scale model that reproduced a wide range of experimental results incorporated a projection from medullary expiratory units to the pons [62] as is present in our model, while additional medullary-pontine and intra-pontine interactions that we included are also based on previous work combining experiments and theory [23, 53, 24, 12]. Our model incorporates a simplified representation of feedback pathways through the NTS that are known to provide inhibitory inputs to the pons [26, 39], with additional control provided by sources of tonic drive in the medulla and pons [6, 66]. The reduced modeling framework that we utilized has been shown in several previous studies of respiratory and locomotor circuits to match, qualitatively and in some cases quantitatively, the activity of large-scale, detailed computational model networks and to reproduce experimentally observed features of rhythmic outputs [60, 59, 49, 10, 19, 8]. The model in this work, despite its simplicity, produces the respiratory patterns associated with eupnea and vagotomy and also reproduces the finding that glutamate injection to the KF can prolong expiration, with a stronger effect in RTT than in control conditions [5]. In all of the models developed in this work, once inhibition to the KF is decreased sufficiently, the expiratory period increases rather abruptly, leading first to slowed, regular breathing followed, with additional loss of inhibition, by progressively slower and more variable respiration. The dependence of respiratory pattern on inhibition level to the KF points to a possible factor that could contribute to the variability of respiratory phenotypes across individuals with RTT [35] and could also have implications for intra-individual variabilities of the respiratory phenotype, including differences in breathing during sleep compared to wakefulness [69, 76]. Since our model omits blood gas exchange and detailed feedback pathways, however, it cannot capture shallow breathing effects.

The role of the KF in the inspiration-expiration switch under vagotomized conditions represented a key distinction between the 3p and 4p models that we considered.

There is evidence suggesting that some neurons in the KF start firing at the end of inspiration [68], consistent with the idea that some degree of intrinsic rhythmicity may be present within the pons [55]. Our 3p model incorporates this viewpoint (Fig. 4A-D). This contention is a matter of debate, however, and many models do not incorporate intrinsic pontine rhythmicity (e.g., [50, 12, 56]). Our 4p models illustrate that even in a highly reduced formulation, such rhythmicity need not be present to achieve appropriately timed rhythms under control and vagotomized conditions; in these models, the expiratory BötC unit activates before the KF, while KF activity significantly prolongs expiration (Fig. 4E-H). As a result of these structural differences, several predictions emerge that could be used to test the relative validity of these models. The 3p model predicts that blockade of KF activity would entirely prevent termination of inspiration in vagotomized preparations, whereas a brief expiratory output would still occur in the 4p models. In the 3p model, expiration could also continue slightly beyond the termination of KF activity, since this termination could arise through mechanisms local to the pons. Finally, the 4p models, but not the 3p model, predicts that inspiratory duration should become prolonged along with expiratory duration under vagotomized conditions (Fig. 9). The two 4p models themselves differ in a way that emerges under simulated RTT conditions. In the 4p-e model, the prolonged apneas that result are terminated when the pre-BötC unit activates by escaping from ongoing inhibition from the BötC. In contrast, in the 4p-r model, apneas end when the KF and BötC reduce their activity, releasing the pre-BötC unit to initiate inspiration. This fundamental distinction, illustrated in Figs. 6-7, yields completely opposite predictions about responses to small inputs to the pre-BötC and BötC units in RTT (Fig. 8) that could be tested experimentally.

Despite the current and past success of this reduced modeling framework, our model clearly has a variety of limitations. To focus on the inclusion of pontine components and phase plane analysis, we omitted fast spiking currents, noting that past works have shown similar rhythmic behaviors from the spiking and non-spiking frameworks (e.g., [60, 49, 10, 9]); future work should consider effects of spiking currents. We also omitted certain features of the respiratory circuit entirely, such as inhibitory neurons within the pre-BötC that may play a role in modulating its activity [11, 56] and the augmenting-expiratory population that extends expiration in more quantitatively accurate models (e.g., [61, 66, 41, 50]). With the latter omission, we felt it was not appropriate to explore recruitment of abdominal outputs and forced expiration such as in hypercapnia, as has been discussed by others [47, 59, 51, 56] and as has recently been explored in connection with the KF [12]. This omission also limits the utility of our current model to study how the durations of inspiration and expiration and the overall respiratory period will

change with modulation of tonic drive strengths, as done in previous work [60]. For example, in our 4p models, the BötC unit must escape from the inhibitory influence of the pre-BötC to initate expiration in order to obtain appropriate rhythmicity in both eupneic and vagotomized conditions, and this reliance on escape, rather than active release initiated by the pre-BötC, could alter frequency responses to changes in inputs. This assumption is, in fact, consistent with the existence of a rhythmic post-inspiratory complex [7, 56]; note that while our BötC unit included a persistent sodium current, the unit's intrinsic dynamics differed across models and tonic drive levels (see Table 1). Moreover, this assumption does not impact the relevance of our model for our goals of studying effects of reduction inhibition to the KF and of 5-HT_{1A} agonist application.

Another limitation of this work is that while we checked that our major findings are robust to local variations in model parameter values, we did not do a global exploration of parameter space. The quantitative details of how respiratory periods change with loss of inhibition to the KF (Fig. 5) may be characteristic of the tuning that we used for our model, and variations may arise with other tunings that produce reasonable eupneic and vagotomized outputs. Thus, experimental testing of these specific details should not be employed to arbitrate between or rule out our models entirely, but rather to evaluate the validity of our models with the particular parameter tunings used in this paper. Furthermore, we do not claim that reduced inhibition to the KF is the only factor in respiratory disruptions associated with RTT. Our model simply provides a principled demonstration that this reduction may suffice to induce the disruptions, and it yields novel predictions about possible changes in activity as this inhibition is gradually reduced.

Indeed, several other possible mechanisms could contribute to experimental observations that were beyond the scope of our reduced models. We did not explicitly model separate GABAergic and glycinergic inhibitory populations and hence did not test possible 5-HT_{1A} agonist effects on the open probability of glycinergic channels [44]; however, evidence supporting the extrapolation of these effects to the full respiratory network or to the KF is so far lacking [58]. We also did not consider the role of endogenous serotonergic drive in the KF and elsewhere. It is well established that patients with RTT have reduced serotonergic metabolites in their cerebral spinal fluid [63]. It is possible that diminished endogenous serotonergic drive itself could contribute to KF overdrive and breathing instability as demonstrated in some experimental settings [57, 22]. Another significant simplification in our model was our representation of the feedback pathways in the respiratory circuit, the details of which are still being determined experimentally. It would be reasonable to infer that in patients with RTT, chronic exposure to intermittent hypoxia could cause maladaptive changes, independent from MeCP2 de-

ficiency, which could contribute to the instability of the rCPG. It is well established that exposure to chronic intermittent hypoxia (such as in obstructive sleep apnoea) promotes carotid body hyperreflexia and hypertonicity (reviewed elsewhere [33]). Chronic exposure to hypoxia has also been shown to produce serotonin-dependent plastic potentiation of centrally integrated peripheral chemoreceptor input [42]. This notion is corroborated by the observation that mouse models of RTT have enhanced ventilatory responses to hypoxia. However, confirmatory human data is lacking [14], and the contribution of these mechanisms to RTT breathing pathology is less clear since hyperoxia, which unloads peripheral chemoreceptors, did not improve periodic breathing in MeCP2 deficient mice [13].

Finally, the current model also omits the possible contribution of glia to the RTT pathology. For instance, it was demonstrated that CO_2-induced calcium currents were dramatically reduced in MeCP2 deficient astrocytes in the ventral medulla [72]. Medullary astrocytes can contribute to RTN-mediated ventilatory responses to CO_2 in vivo [31]. Indeed, MeCP2-deficient mice have impaired hypercapnic ventilatory responses and elevated apnoeic thresholds [71, 14]. Moreover, the conditional depletion of MeCP2 in astrocytes alone recapitulated the blunted CO_2 sensitivity phenotype [29]. Interestingly, re-expression of MeCP2 either in glia or in GABAergic neurons alone sufficed to ameliorate the breathing phenotype in mouse models of RTT [43, 73]. This result is consistent with the idea that the balance of drives to expiratory versus inspiratory neuron populations is the most important component of the breathing instability in RTT, a feature that is reproduced by our model.

Reduced models have recently served as useful tools in testing theories of respiratory rhythm generation and control. The results that we obtained by harnessing this framework add support for the ideas that a reduction in inhibition to the KF may play a significant role in producing the disordered respiration associated with RTT, while application of 5-HT_{1A} agonists in RTT conditions may enhance respiratory function through contributions of 5-HT_{1A}-sensitive potassium currents or other hyperpolarizing effects. Our findings highlight the importance of future experiments to continue to explore these ideas and suggest possible directions for these experiments to pursue.

References

[1] ClinicalTrials.gov [Internet]. Bethesda (MD): National Library of Medicine (US). 2016 June 3 - Identifier NCT02790034, Evaluation of the Efficacy, Safety, and Tolerability of Sarizotan in Rett Syndrome With Respiratory Symptoms. 2018 Sep 11 [cited 2018 Dec 8]; [about 6 screens]. Available from: https://clinicaltrials.gov/ct2/show/NCT02790034?term=sarizotan&rank=1.

[2] Abdala, A. P., Bissonnette, J. M., and Newman-Tancredi, A. Pinpointing brainstem mechanisms responsible for autonomic dysfunction in Rett syndrome: therapeutic perspectives for 5-HT1A agonists. *Frontiers in Physiology 5* (2014), 205.

[3] Abdala, A. P., Dutschmann, M., Bissonnette, J. M., and Paton, J. F. Correction of respiratory disorders in a mouse model of Rett syndrome. *Proceedings of the National Academy of Sciences 107*, 42 (2010), 18208–18213.

[4] Abdala, A. P., Lioy, D. T., Garg, S. K., Knopp, S. J., Paton, J. F., and Bissonnette, J. M. Effect of Sarizotan, a 5-HT1a and D2-like receptor agonist, on respiration in three mouse models of Rett syndrome. *American journal of respiratory cell and molecular biology 50*, 6 (2014), 1031–1039.

[5] Abdala, A. P., Toward, M. A., Dutschmann, M., Bissonnette, J. M., and Paton, J. F. Deficiency of GABAergic synaptic inhibition in the Kölliker–Fuse area underlies respiratory dysrhythmia in a mouse model of Rett syndrome. *The Journal of Physiology 594*, 1 (2016), 223–237.

[6] Alheid, G. F., Milsom, W. K., and McCrimmon, D. R. Pontine influences on breathing: an overview. *Respiratory Physiology & Neurobiology 143*, 2-3 (2004), 105–114.

[7] Anderson, T. M., Garcia, A. J., Baertsch, N. A., Pollak, J., Bloom, J. C., Wei, A. D., Rai, K. G., and Ramirez, J.-M. A novel excitatory network for the control of breathing. *Nature 536*, 7614 (2016), 76.

[8] Ausborn, J., Koizumi, H., Barnett, W. H., John, T. T., Zhang, R., Molkov, Y. I., Smith, J. C., and Rybak, I. A. Organization of the core respiratory network: Insights from optogenetic and modeling studies. *PLoS Computational Biology 14*, 4 (2018), e1006148.

[9] Ausborn, J., Snyder, A. C., Shevtsova, N. A., Rybak, I. A., and Rubin, J. E. State-dependent rhythmogenesis and frequency control in a half-center locomotor CPG. *Journal of Neurophysiology 119*, 1 (2017), 96–117.

[10] Bacak, B. J., Kim, T., Smith, J. C., Rubin, J. E., and Rybak, I. A. Mixed-mode oscillations and population bursting in the pre-Bötzinger complex. *eLife 5* (2016), e13403.

[11] Baertsch, N. A., Baertsch, H. C., and Ramirez, J. M. The interdependence of excitation and inhibition for the control of dynamic breathing rhythms. *Nature Communications 9*, 1 (2018), 843.

[12] Barnett, W. H., Jenkin, S. E., Milsom, W. K., Paton, J. F., Abdala, A. P., Molkov, Y. I., and Zoccal, D. B. The Kölliker-Fuse nucleus orchestrates the timing of expiratory abdominal nerve bursting. *Journal of Neurophysiology 119*, 2 (2018), 401–412.

[13] Bissonnette, J. M., and Knopp, S. J. Effect of inspired oxygen on periodic breathing in methy-CpG-binding protein 2 (Mecp2) deficient mice. *Journal of Applied Physiology 104*, 1 (2008), 198–204.

[14] Bissonnette, J. M., Schaevitz, L. R., Knopp, S. J., and Zhou, Z. Respiratory phenotypes are distinctly affected in mice with common Rett syndrome mutations MeCP2 T158A and R168X. *Neuroscience 267* (2014), 166–176.

[15] Butera, R., Rinzel, J., and Smith, J. Models of respiratory rhythm generation in the pre-Bötzinger complex. I. Bursting pacemaker neurons. *J. Neurophysiol. 81* (1999), 382–397.

[16] Chao, H.-T., Chen, H., Samaco, R. C., Xue, M., Chahrour, M., Yoo, J., Neul, J. L., Gong, S., Lu, H.-C., Heintz, N., et al. Dysfunction in gaba signalling mediates autism-like stereotypies and Rett syndrome phenotypes. *Nature 468*, 7321 (2010), 263.

[17] Cohen, M. I. Switching of the respiratory phases and evoked phrenic responses produced by rostral pontine electrical stimulation. *The Journal of Physiology 217*, 1 (1971), 133–158.

[18] Connelly, C. A., Otto-Smith, M. R., and Feldman, J. L. Blockade of NMDA receptor-channels by MK-801 alters breathing in adult rats. *Brain Research 596*, 1-2 (1992), 99–110.

[19] Danner, S. M., Shevtsova, N. A., Frigon, A., and Rybak, I. A. Computational modeling of spinal circuits controlling limb coordination and gaits in quadrupeds. *eLife 6* (2017), e31050.

[20] Daun, S., Rubin, J. E., and Rybak, I. A. Control of oscillation periods and phase durations in half-center central pattern generators: a comparative mechanistic analysis. *Journal of Computational Neuroscience 27*, 1 (2009), 3.

[21] Del Negro, C. A., Wilson, C. G., Butera, R. J., Rigatto, H., and Smith, J. C. Periodicity, mixed-mode oscillations, and quasiperiodicity in a rhythm-generating neural network. *Biophysical Journal 82*, 1 (2002), 206–214.

[22] Dhingra, R., Dutschmann, M., and Dick, T. Blockade of dorsolateral pontine 5HT1A receptors destabilizes the respiratory rhythm in C57BL6/J wild-type mice. *Respiratory Physiology & Neurobiology 226* (2016), 110–114.

[23] Dick, T. E., Shannon, R., Lindsey, B. G., Nuding, S. C., Segers, L. S., Baekey, D. M., and Morris, K. F. Pontine respiratory-modulated activity before and after vagotomy in decerebrate cats. *The Journal of Physiology 586*, 17 (2008), 4265–4282.

[24] Dutschmann, M., and Dick, T. E. Pontine mechanisms of respiratory control. *Comprehensive Physiology 2*, 4 (2012), 2443.

[25] Ermentrout, B. *Simulating, analyzing, and animating dynamical systems: a guide to XPPAUT for researchers and students*, vol. 14. SIAM, 2002.

[26] Ezure, K., and Tanaka, I. GABA, in some cases together with glycine, is used as the inhibitory transmitter by pump cells in the Hering-Breuer reflex pathway of the rat. *Neuroscience 127*, 2 (2004), 409–417.

[27] Ezure, K., Tanaka, I., and Kondo, M. Glycine is used as a transmitter by decrementing expiratory neurons of the ventrolateral medulla in the rat. *Journal of Neuroscience 23*, 26 (2003), 8941–8948.

[28] Ezure, K., Tanaka, I., and Saito, Y. Brainstem and spinal projections of augmenting expiratory neurons in the rat. *Neuroscience Research 45*, 1 (2003), 41–51.

[29] Garg, S. K., Lioy, D. T., Knopp, S. J., and Bissonnette, J. M. Conditional depletion of methyl-CpG-binding protein 2 in astrocytes depresses the

hypercapnic ventilatory response in mice. *Journal of Applied Physiology 119*, 6 (2015), 670–676.

[30] Getting, P. A. Emerging principles governing the operation of neural networks. *Annual Review of Neuroscience 12*, 1 (1989), 185–204.

[31] Guyenet, P. G., and Bayliss, D. A. Neural control of breathing and CO2 homeostasis. *Neuron 87*, 5 (2015), 946–961.

[32] Harris, K. D., Dashevskiy, T., Mendoza, J., Garcia III, A. J., Ramirez, J.-M., and Shea-Brown, E. Different roles for inhibition in the rhythm-generating respiratory network. *Journal of Neurophysiology 118*, 4 (2017), 2070–2088.

[33] Iturriaga, R., Oyarce, M. P., and Dias, A. C. R. Role of carotid body in intermittent hypoxia-related hypertension. *Current Hypertension Reports 19*, 5 (2017), 38.

[34] Izhikevich, E. M. *Dynamical systems in neuroscience*. MIT press, 2007.

[35] Julu, P. O., Engerström, I. W., Hansen, S., Apartopoulos, F., Engerström, B., Pini, G., Delamont, R. S., and Smeets, E. E. Cardiorespiratory challenges in Rett's syndrome. *The Lancet 371*, 9629 (2008), 1981–1983.

[36] Kline, D. D., Ogier, M., Kunze, D. L., and Katz, D. M. Exogenous brain-derived neurotrophic factor rescues synaptic dysfunction in Mecp2-null mice. *Journal of Neuroscience 30*, 15 (2010), 5303–5310.

[37] Koizumi, H., Wilson, C., Wong, S., Yamanishi, T., Koshiya, N., and Smith, J. Functional imaging, spatial reconstruction, and biophysical analysis of a respiratory motor circuit isolated *in vitro*. *J. Neurosci. 28* (2008), 2353–2365.

[38] Kron, M., Lang, M., Adams, I. T., Sceniak, M., Longo, F., and Katz, D. M. A bdnf loop-domain mimetic acutely reverses spontaneous apneas and respiratory abnormalities during behavioral arousal in a mouse model of Rett syndrome. *Disease Models & Mechanisms 7*, 9 (2014), 1047–1055.

[39] Kubin, L., Alheid, G. F., Zuperku, E. J., and McCrimmon, D. R. Central pathways of pulmonary and lower airway vagal afferents. *Journal of Applied Physiology 101*, 2 (2006), 618–627.

[40] Levitt, E. S., Hunnicutt, B. J., Knopp, S. J., Williams, J. T., and Bissonnette, J. M. A selective 5-HT1a receptor agonist improves respiration in a mouse model of Rett syndrome. *Journal of Applied Physiology 115*, 11 (2013), 1626–1633.

[41] Lindsey, B. G., Rybak, I. A., and Smith, J. C. Computational models and emergent properties of respiratory neural networks. *Comprehensive Physiology 2*, 3 (2012), 1619.

[42] Ling, L., Fuller, D. D., Bach, K. B., Kinkead, R., Olson, E. B., and Mitchell, G. S. Chronic intermittent hypoxia elicits serotonin-dependent plasticity in the central neural control of breathing. *Journal of Neuroscience 21*, 14 (2001), 5381–5388.

[43] Lioy, D. T., Garg, S. K., Monaghan, C. E., Raber, J., Foust, K. D., Kaspar, B. K., Hirrlinger, P. G., Kirchhoff, F., Bissonnette, J. M., Ballas, N., et al. A role for glia in the progression of Retts syndrome. *Nature 475*, 7357 (2011), 497.

[44] Manzke, T., Niebert, M., Koch, U. R., Caley, A., Vogelgesang, S., Hülsmann, S., Ponimaskin, E., Müller, U., Smart, T. G., Harvey, R. J., et al. Serotonin receptor 1a–modulated phosphorylation of glycine receptor $\alpha 3$ controls breathing in mice. *The Journal of Clinical Investigation 120*, 11 (2010), 4118–4128.

[45] Marchenko, V., Koizumi, H., Mosher, B., Koshiya, N., Tariq, M. F., Bezdudnaya, T. G., Zhang, R., Molkov, Y. I., Rybak, I. A., and Smith, J. C. Perturbations of respiratory rhythm and pattern by disrupting synaptic inhibition within pre-Bötzinger and Bötzinger complexes. *eNeuro* (2016), ENEURO–0011.

[46] Medrihan, L., Tantalaki, E., Aramuni, G., Sargsyan, V., Dudanova, I., Missler, M., and Zhang, W. Early defects of GABAergic synapses in the brain stem of a MeCP2 mouse model of rett syndrome. *Journal of Neurophysiology 99*, 1 (2008), 112–121.

[47] Molkov, Y. I., Abdala, A. P., Bacak, B. J., Smith, J. C., Paton, J. F., and Rybak, I. A. Late-expiratory activity: emergence and interactions with the respiratory CPG. *Journal of Neurophysiology 104*, 5 (2010), 2713–2729.

[48] Molkov, Y. I., Bacak, B. J., Dick, T. E., and Rybak, I. A. Control of breathing by interacting pontine and pulmonary feedback loops. *Frontiers in Neural Circuits 7* (2013), 16.

[49] Molkov, Y. I., Bacak, B. J., Talpalar, A. E., and Rybak, I. A. Mechanisms of left-right coordination in mammalian locomotor pattern generation circuits: a mathematical modeling view. *PLoS Computational Biology 11*, 5 (2015), e1004270.

[50] Molkov, Y. I., Rubin, J. E., Rybak, I. A., and Smith, J. C. Computational models of the neural control of breathing. *Wiley Interdisciplinary Reviews: Systems Biology and Medicine 9*, 2 (2017), e1371.

[51] Molkov, Y. I., Shevtsova, N. A., Park, C., Ben-Tal, A., Smith, J. C., Rubin, J. E., and Rybak, I. A. A closed-loop model of the respiratory system: focus on hypercapnia and active expiration. *PLoS One 9*, 10 (2014), e109894.

[52] Monteau, R., Gauthier, P., Rega, P., and Hilaire, G. Effects of N-methyl–aspartate (NMDA) antagonist MK-801 on breathing pattern in rats. *Neuroscience Letters 109*, 1-2 (1990), 134–139.

[53] Mörschel, M., and Dutschmann, M. Pontine respiratory activity involved in inspiratory/expiratory phase transition. *Philosophical Transactions of the Royal Society of London B: Biological Sciences 364*, 1529 (2009), 2517–2526.

[54] Okazaki, M., Takeda, R., Yamazaki, H., and Haji, A. Synaptic mechanisms of inspiratory off-switching evoked by pontine pneumotaxic stimulation in cats. *Neuroscience Research 44*, 1 (2002), 101–110.

[55] Poon, C.-S., and Song, G. Bidirectional plasticity of pontine pneumotaxic postinspiratory drive: implication for a pontomedullary respiratory central pattern generator. In *Progress in Brain Research*, vol. 209. Elsevier, 2014, pp. 235–254.

[56] Ramirez, J.-M., and Baertsch, N. A. The dynamic basis of respiratory rhythm generation: One breath at a time. *Annual Review of Neuroscience 41* (2018), 475–499.

[57] Richter, D. W., Manzke, T., Wilken, B., and Ponimaskin, E. Serotonin receptors: guardians of stable breathing. *Trends in Molecular Medicine 9*, 12 (2003), 542–548.

[58] Rojas, P. S., and Fiedler, J. L. What do we really know about 5-HT1A receptor signaling in neuronal cells? *Frontiers in Cellular Neuroscience 10* (2016), 272.

[59] Rubin, J. E., Bacak, B. J., Molkov, Y. I., Shevtsova, N. A., Smith, J. C., and Rybak, I. A. Interacting oscillations in neural control of breathing: modeling and qualitative analysis. *Journal of Computational Neuroscience 30*, 3 (2011), 607–632.

[60] Rubin, J. E., Shevtsova, N. A., Ermentrout, G. B., Smith, J. C., and Rybak, I. A. Multiple rhythmic states in a model of the respiratory central pattern generator. *Journal of Neurophysiology 101*, 4 (2009), 2146–2165.

[61] Rybak, I. A., Abdala, A. P., Markin, S. N., Paton, J. F., and Smith, J. C. Spatial organization and state-dependent mechanisms for respiratory rhythm and pattern generation. *Progress in Brain Research 165* (2007), 201–220.

[62] Rybak, I. A., O'connor, R., Ross, A., Shevtsova, N., Nuding, S. C., Segers, L. S., Shannon, R., Dick, T. E., Dunin-Barkowski, W. L., Orem, J. M., et al. Reconfiguration of the pontomedullary respiratory network: a computational modeling study with coordinated in vivo experiments. *Journal of Neurophysiology 100*, 4 (2008), 1770–1799.

[63] Samaco, R. C., Mandel-Brehm, C., Chao, H.-T., Ward, C. S., Fyffe-Maricich, S. L., Ren, J., Hyland, K., Thaller, C., Maricich, S. M., Humphreys, P., et al. Loss of MeCP2 in aminergic neurons causes cell-autonomous defects in neurotransmitter synthesis and specific behavioral abnormalities. *Proceedings of the National Academy of Sciences* (2009), pnas–0912257106.

[64] Shevtsova, N. A., Manzke, T., Molkov, Y. I., Bischoff, A., Smith, J. C., Rybak, I. A., and Richter, D. W. Computational modelling of 5-HT receptor-mediated reorganization of the brainstem respiratory network. *European Journal of Neuroscience 34*, 8 (2011), 1276–1291.

[65] Skinner, F. K., Kopell, N., and Marder, E. Mechanisms for oscillation and frequency control in reciprocally inhibitory model neural networks. *Journal of Computational Neuroscience 1*, 1-2 (1994), 69–87.

[66] Smith, J. C., Abdala, A., Koizumi, H., Rybak, I. A., and Paton, J. F. Spatial and functional architecture of the mammalian brain stem respiratory network: a hierarchy of three oscillatory mechanisms. *Journal of Neurophysiology 98*, 6 (2007), 3370–3387.

[67] Smith, J. C., Abdala, A. P., Borgmann, A., Rybak, I. A., and Paton, J. F. Brainstem respiratory networks: building blocks and microcircuits. *Trends in Neurosciences 36*, 3 (2013), 152–162.

[68] Song, G., Tin, C., and Poon, C.-S. Multiscale fingerprinting of neuronal functional connectivity. *Brain Structure and Function 220*, 5 (2015), 2967–2982.

[69] Southall, D., Kerr, A., Tirosh, E., Amos, P., Lang, M., and Stephenson, J. Hyperventilation in the awake state: potentially treatable component of Rett syndrome. *Archives of Disease in Childhood 63*, 9 (1988), 1039–1048.

[70] Stettner, G. M., Huppke, P., Brendel, C., Richter, D. W., Gärtner, J., and Dutschmann, M. Breathing dysfunctions associated with impaired control of postinspiratory activity in Mecp2-/y knockout mice. *The Journal of Physiology 579*, 3 (2007), 863–876.

[71] Toward, M. A., Abdala, A. P., Knopp, S. J., Paton, J. F., and Bissonnette, J. M. Increasing brain serotonin corrects CO2 chemosensitivity in methyl-CpG-binding protein 2 (Mecp2)-deficient mice. *Experimental Physiology 98*, 3 (2013), 842–849.

[72] Turovsky, E., Karagiannis, A., Abdala, A. P., and Gourine, A. V. Impaired CO2 sensitivity of astrocytes in a mouse model of Rett syndrome. *The Journal of Physiology 593*, 14 (2015), 3159–3168.

[73] Ure, K., Lu, H., Wang, W., Ito-Ishida, A., Wu, Z., He, L.-j., Sztainberg, Y., Chen, W., Tang, J., and Zoghbi, H. Y. Restoration of Mecp2 expression in GABAergic neurons is sufficient to rescue multiple disease features in a mouse model of Rett syndrome. *eLife 5* (2016), e14198.

[74] Viemari, J.-C., Roux, J.-C., Tryba, A. K., Saywell, V., Burnet, H., Peña, F., Zanella, S., Bévengut, M., Barthelemy-Requin, M., Herzing, L. B., et al. Mecp2 deficiency disrupts norepinephrine and respiratory systems in mice. *Journal of Neuroscience 25*, 50 (2005), 11521–11530.

[75] Wang, X.-J., and Rinzel, J. Alternating and synchronous rhythms in reciprocally inhibitory model neurons. *Neural Computation 4*, 1 (1992), 84–97.

[76] Weese-Mayer, D. E., Lieske, S. P., Boothby, C. M., Kenny, A. S., Bennett, H. L., and Ramirez, J.-M. Autonomic dysregulation in young girls with Rett Syndrome during nighttime in-home recordings. *Pediatric Pulmonology 43*, 11 (2008), 1045–1060.

[77] Weese-Mayer, D. E., Lieske, S. P., Boothby, C. M., Kenny, A. S., Bennett, H. L., Silvestri, J. M., and Ramirez, J.-M. Autonomic nervous system dysregulation: breathing and heart rate perturbation during wakefulness in young girls with Rett syndrome. *Pediatric Research 60*, 4 (2006), 443.

Competing interests: A. Abdala has received contract research funds from Neurolixis, Inc. on unrelated past projects and has provided paid consultancy to Neurolixis Inc. in the past.

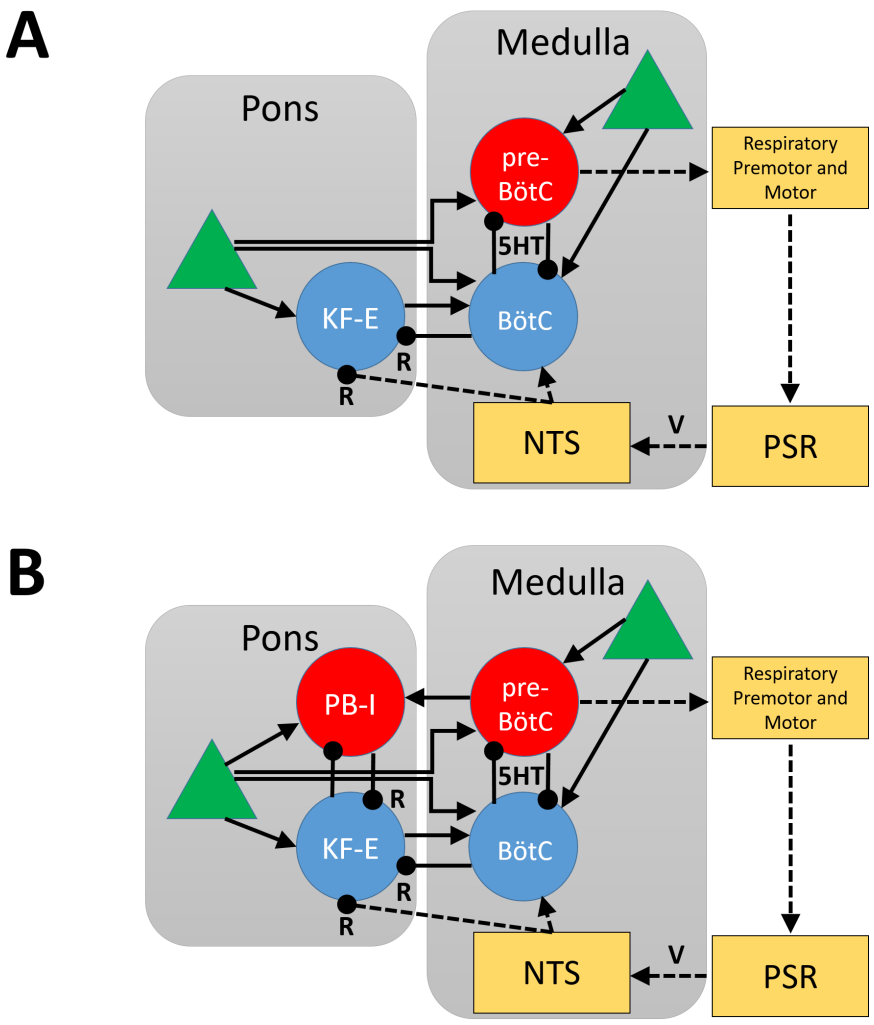

Figure 1: Schematic illustrations of model components. (A) The 3p model includes three populations of potentially active respiratory neurons, representing neurons from the pre-BötC, BötC, and Kölliker-Fuse (KF-E). It also features medullary and pontine sources of tonic excitatory synaptic drive (green triangles). The model includes a simplified representation of pulmonary stretch receptor (PSR) feedback related to pre-BötC output and mediated through the nucleus solitarus (NTS). (B) The 4p-r and 4p-e models share the same structure, which includes the same populations as the 3p model along with an additional parabrachial (PB-I) population. Red circles: active (or more active) during inspriation; blue circles: active (or suppressed) during expiration; connections capped with arrows: excitatory synaptic pathways; connections capped with circles: inhibitory synaptic pathways; V: cut to represent vagotomy; R: altered to represent RTT; 5-HT: altered as part of the representations of 5-HT$_{1A}$ agonist application; yellow boxes and dashed lines: components and pathways that are collapsed into a simplified drive rather modeled separately.

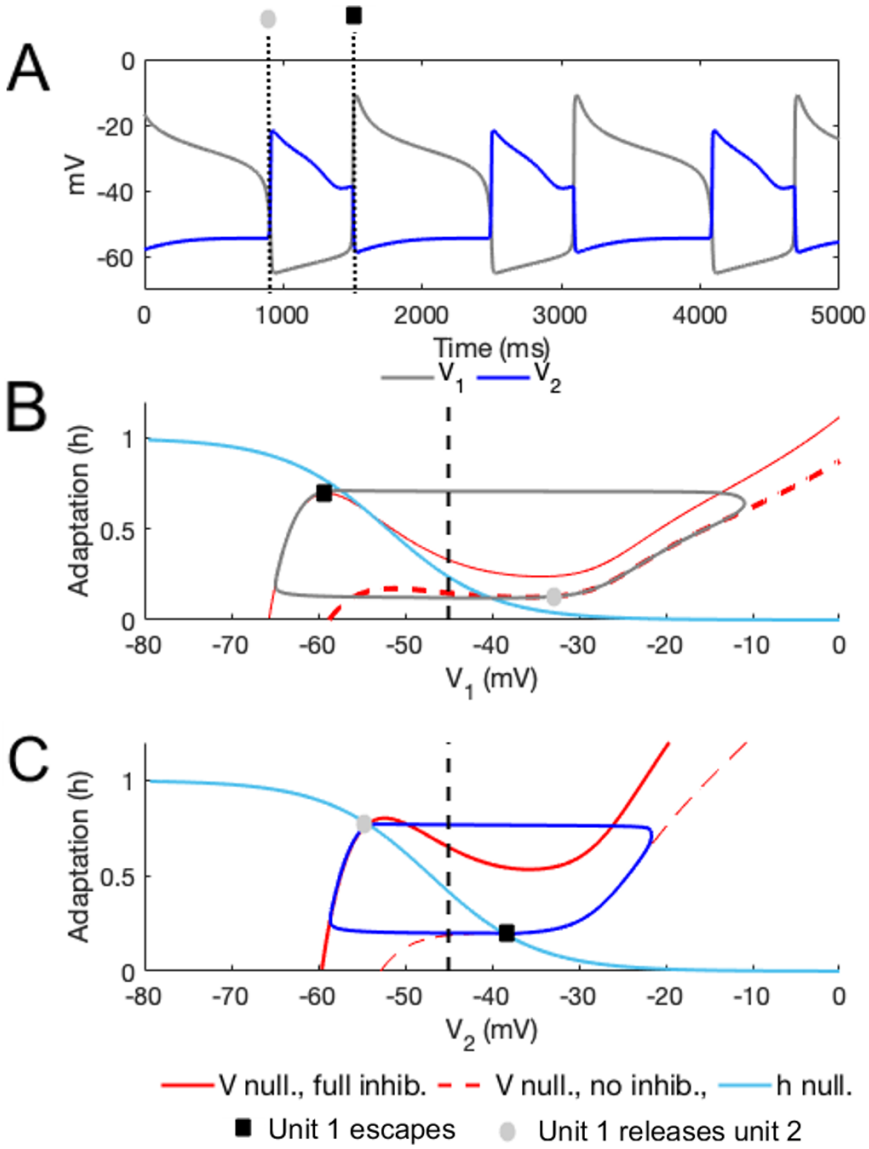

Figure 2: An example simulation involving transitions by escape and release. (A) Voltage time courses for two units coupled by mutual synaptic inhibition. The black square denotes a time when unit 1 activates, while the gray circle marks a time when unit 2 activates. (B) Projection to the phase plane for unit 1. (C) Projection to the phase plane for unit 2. In both phase planes, in addition to the model trajectory (grey in B, blue in C), two V-nullclines are included, one corresponding to the maximal level of inhibition to the unit (solid red) and one corresponding to no inhibition to the unit (dashed red), along with an h-nullcline (cyan). The threshold for synaptic inhibition is also shown (black dashed). See text (Methods) for details.

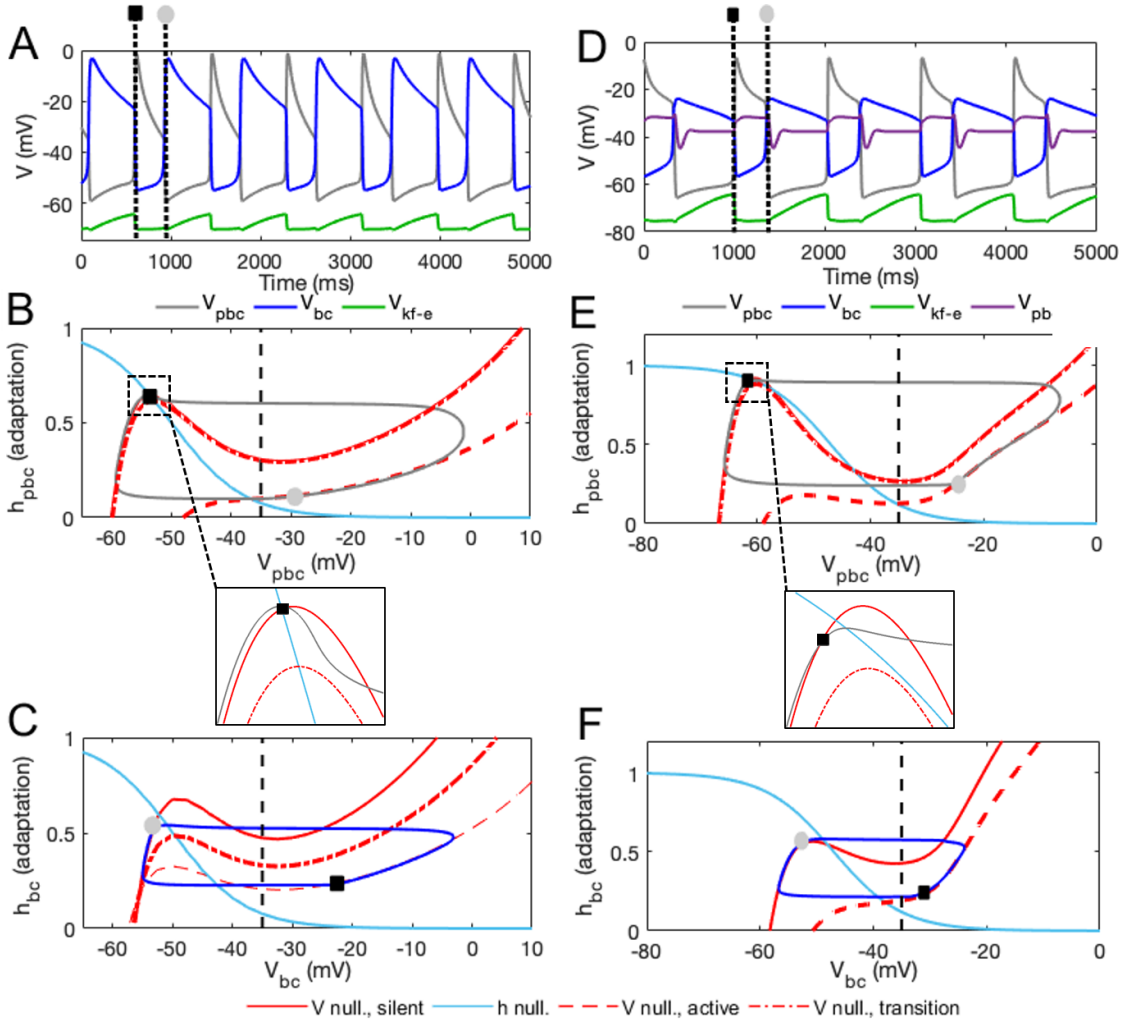

Figure 3: Voltage time courses and phase plane views of intact model outputs in the eupneic state. (A-C) 3p model. (D-F) 4p-r model (4p-e model results are almost identical and are not shown). (A,D) Eupneic output patterns feature a longer BötC expiratory activation period than pre-BötC inspiratory duration as well as pontine suppression (color codes given in legends). The black squares indicate the start of inspiration, the gray circles the start of expiration, in an example cycle. (B,E) Projections to the phase plane for the pre-BötC variables. In each, the trajectory (grey), three V-nullclines (red), and one h-nullcline (cyan) are shown. The solid V-nullcline corresponds to the maximal level of inhibition to the pre-BötC unit, received at the start of its silent phase (i.e., expiration). The dashed V-nullcline applies in the absence of inhibition, corresponding to its active phase (i.e., inspiration). The dash-dotted V-nullcline corresponds to the level of inhibition received when the pre-BötC unit starts to transition to the active phase (at the moment indicated by the black square). The vertical dashed black line indicates the synaptic threshold $\theta_{syn_{pbc,bc}}$ (see Methods). The dash-dotted nullclines are almost indistinguishable from the solid ones, except in the insets. (C,F) Projections to the phase plane for the BötC variables. Nullcline coding is the same except that the solid V-nullcline now corresponds to the start of inspiration, the dashed to the start of expiration, and the dash-dotted to the start of the transition to expiration (at the moment indicated by the gray circle), such that the legend is correct for panels B,C,E, and F. The vertical dashed black line indicates the synaptic threshold $\theta_{syn_{bc,pbc}}$.

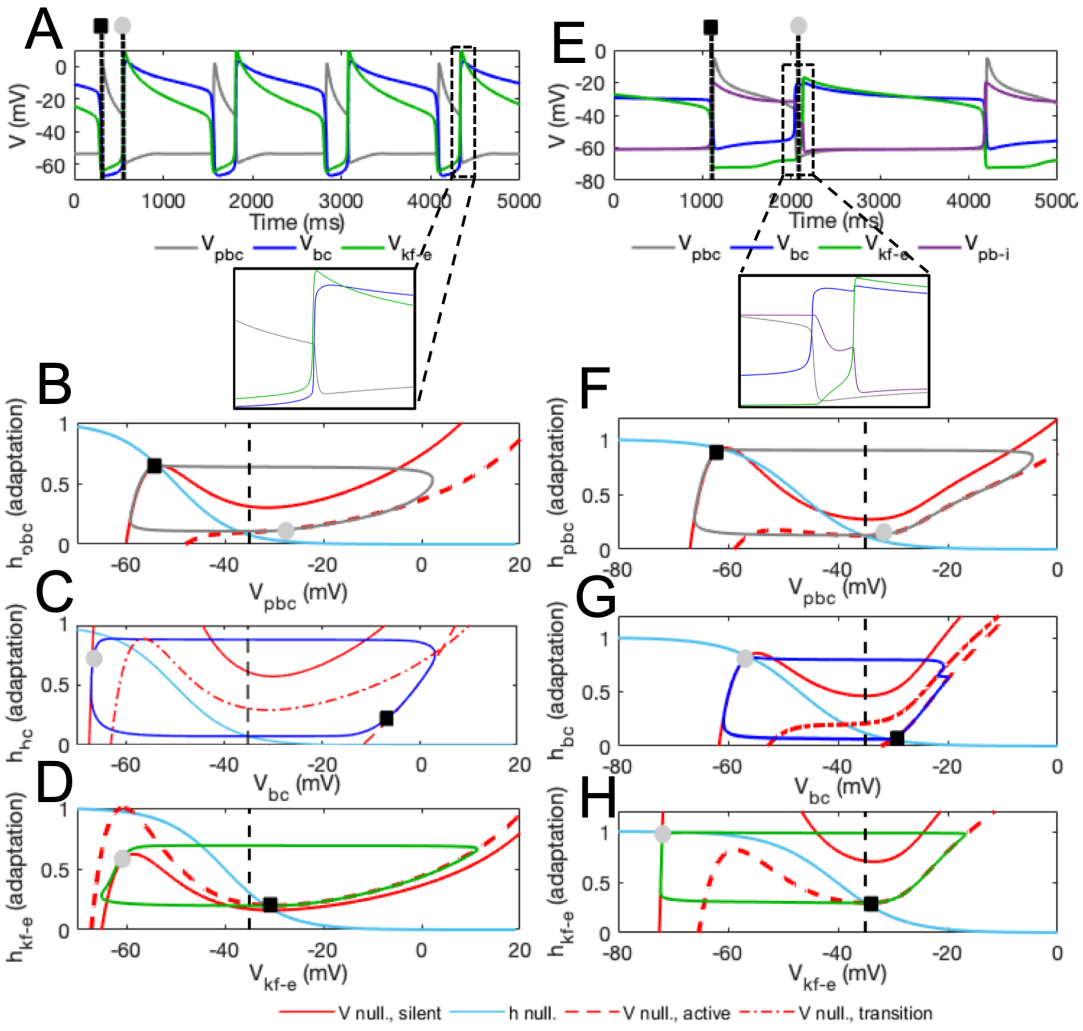

Figure 4: Voltage time courses and phase plane views of vagotomized model outputs in the eupneic state. Color codes and labels as in Fig. 3. (A-D) 3p model. (E-H) 4p-r model (4p-e model results are almost identical and are not shown). (A,E) Eupneic outputs under vagotomy feature a longer expiratory phase and ratio of expiratory duration to inspiratory duration than in the intact case (Fig. 3), with rhythmic KF-E and PB-I alternation that is absent in the intact case. Insets show that in the 3p model, KF-E activation occurs at the start of expiration (A) while in the 4p models, it follows BötC activation. (B,F) Projections to the pre-BötC phase plane. (C,G) Projections to the BötC phase plane. (D,H) Projections to the KF-E phase plane. The solid V-nullcline corresponds to the level of inhibition received during inspiration, the dashed V-nullcline to the level received during expiration.

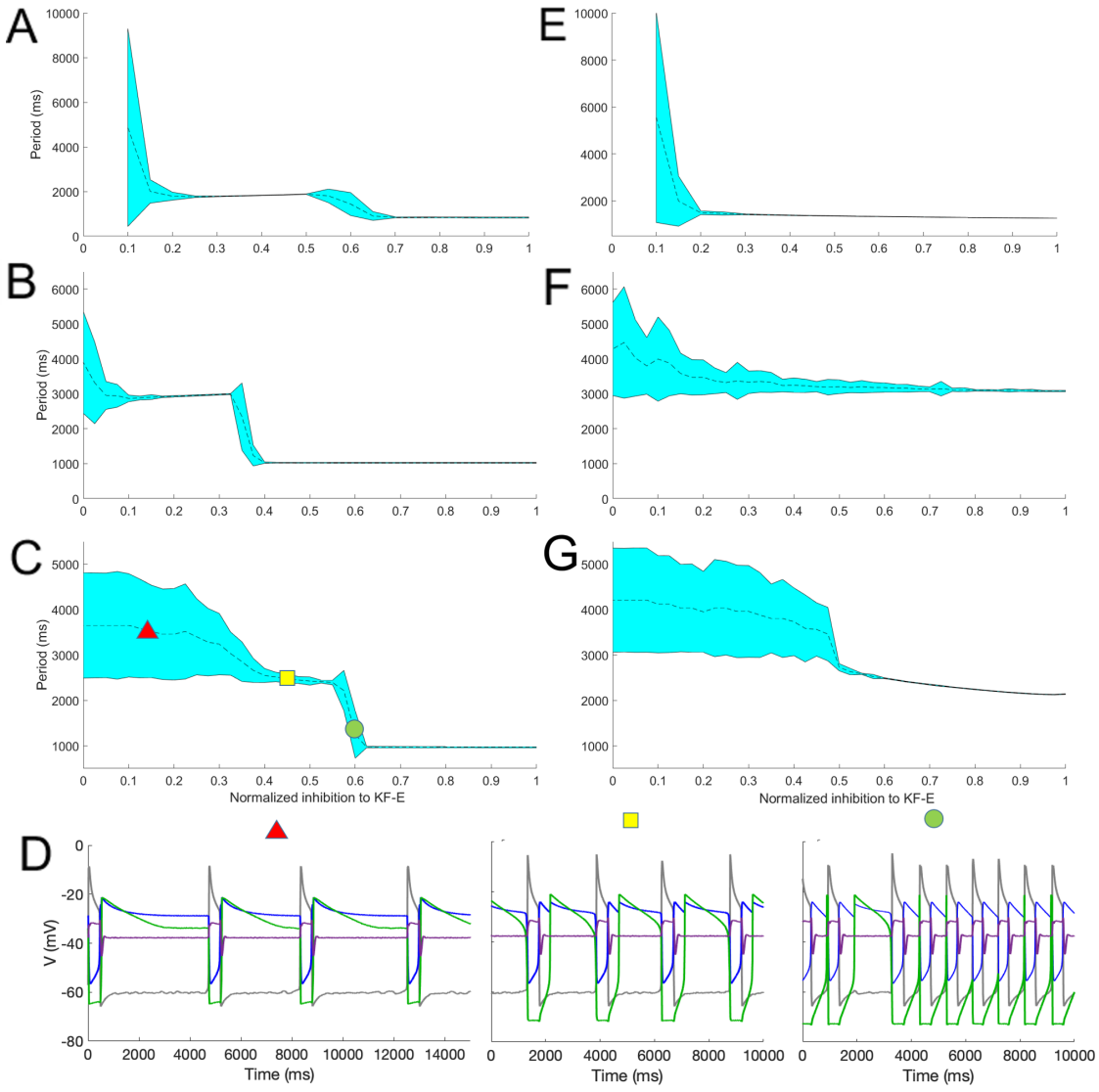

Figure 5: Reduction in inhibition to the KF-E unit leads to increased duration and variability of the respiratory cycle period due to increased expiratory phase durations and variability associated with prolonged KF-E activation. (A-C) Period as a function of fraction of inhibition to the KF-E that is present, relative to the baseline model, in the intact case. The blue curves denote averages while the cyan clouds represent the standard deviations. (A) 3p model. (B) 4p-r model. (C) 4p-e model. (D) Example voltage time courses for the 4p-e model for the inhibition levels marked with a green circle, yellow square, and red triangle, respectively, in (C). Color codes as in Fig. 4. (D-F) Periods as a function of fraction of inhibition to the KF-E that is present, relative to the baseline model, in the vagotomized case.

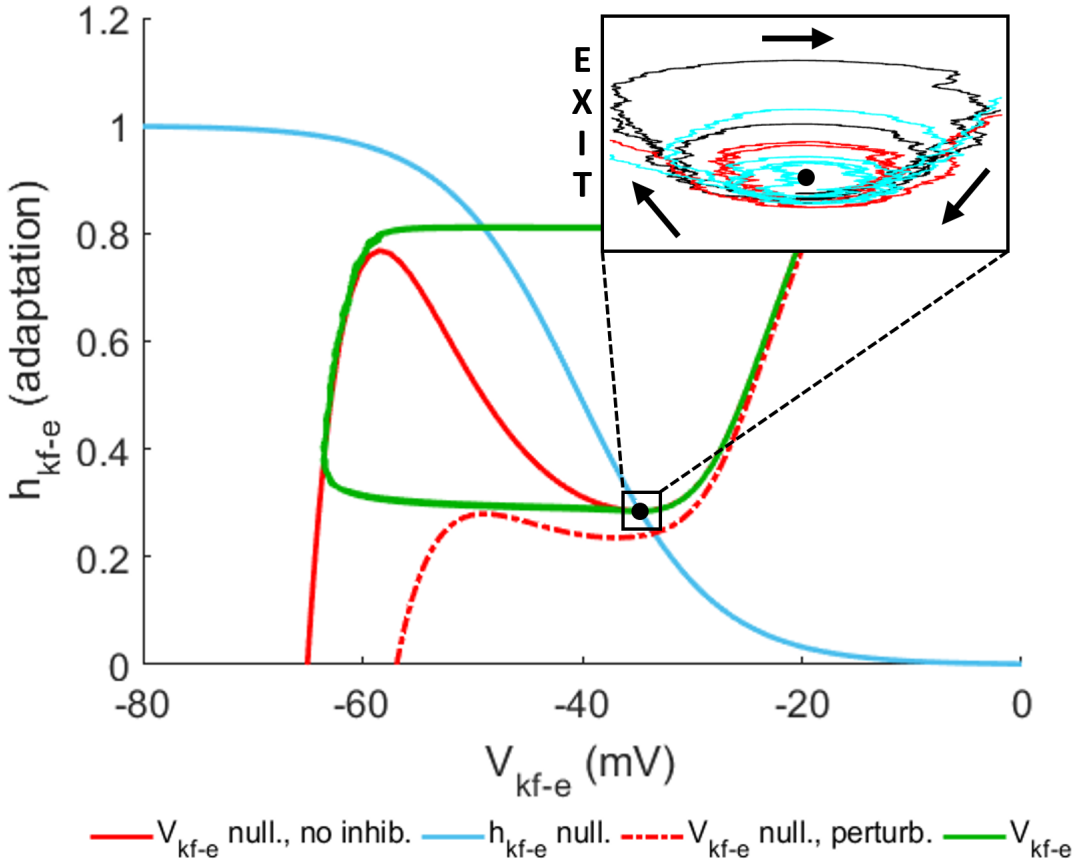

Figure 6: Simulation of severe RTT results in a stable equilibrium point with sustained KF-E activation. In the projection to the KF-E phase plane, the V-nullcline that is relevant during expiration (solid red) intersects the h-nullcline (cyan) on the right branch of the V-nullcline, yielding a stable equilibrium point (black circle). The figure also includes a projected cycle of an apneic solution (green) and the V-nullcline corresponding to the application of a small, depolarizing current to the KF-E unit (dash-dotted red). Inset: A zoomed view near the equilibrium point reveals that the projection of the model output winds around this equilibrium due to noise (arrows show direction of net rotation). On each cycle, if fluctuations pull voltage low enough (far enough to the left), then a transition out of expiration will result (from region marked "EXIT"). Otherwise, another cycle must occur before this transition can be possible. Successive expiratory phases, each consisting of multiple cycles, are colored black, cyan, and red.

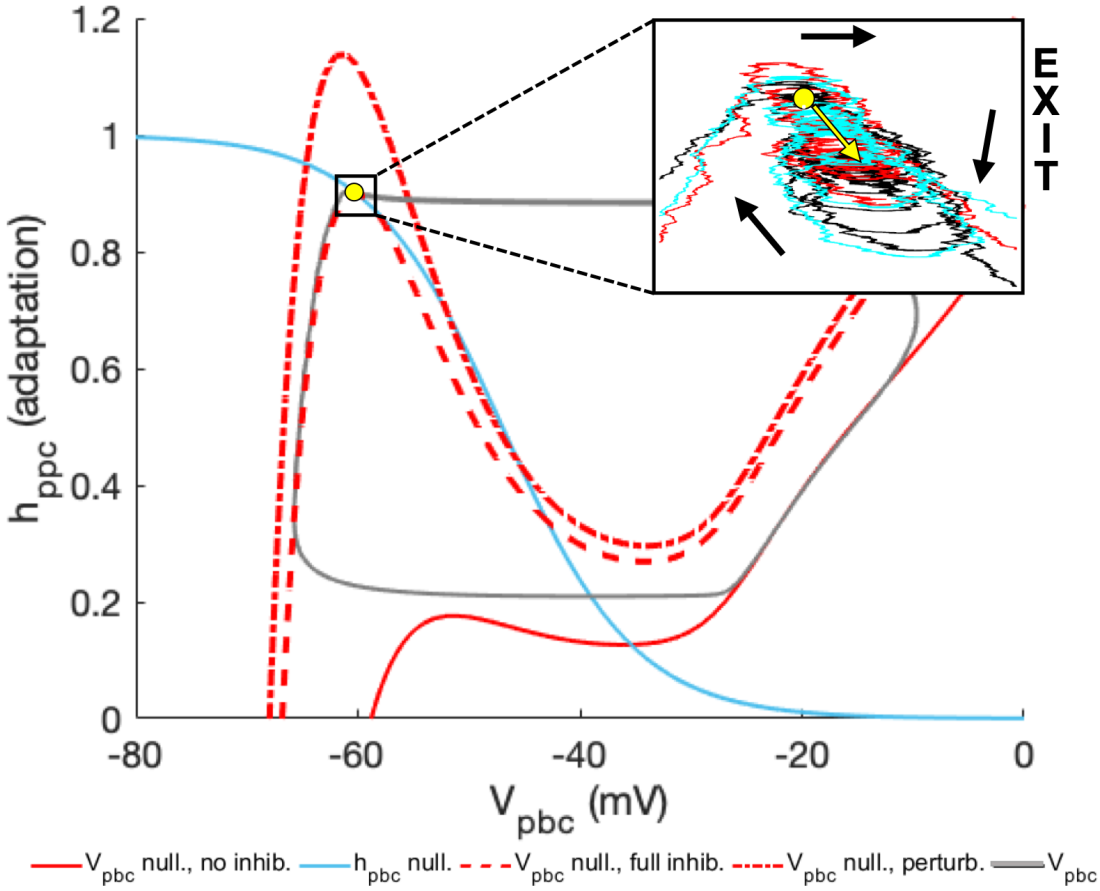

Figure 7: Simulation of severe RTT results in a stable equilibrium point with sustained pre-BötC suppression. In the projection to the pre-BötC phase plane, the V-nullcline that is relevant at the start of expiration (dashed red) intersects the h-nullcline (cyan) on the left branch of the V-nullcline, yielding a stable equilibrium point (yellow circle). The figure also includes a projected cycle of an apneic solution (grey), the V-nullcline relevant during inspiration (solid red), and the V-nullcline corresponding to the application of a small, hyperpolarizing current to the pre-BötC unit (dash-dotted red). Inset: A zoomed view near the equilibrium point reveals that the projection of the model output winds locally due to noise (arrows show direction of net rotation); furthermore, the V-nulllcline location and hence the equilibrium location as well drift to larger V and smaller h due to gradual adaption of BötC activity and decrease of inhibition. On each cycle, if fluctuations pull voltage high enough (far enough to the right), then a transition into inspiration will result (from region marked "EXIT"). Otherwise, another cycle must occur before this transition can be possible. Successive expiratory phases, each consisting of multiple cycles, are colored black, cyan, and red.

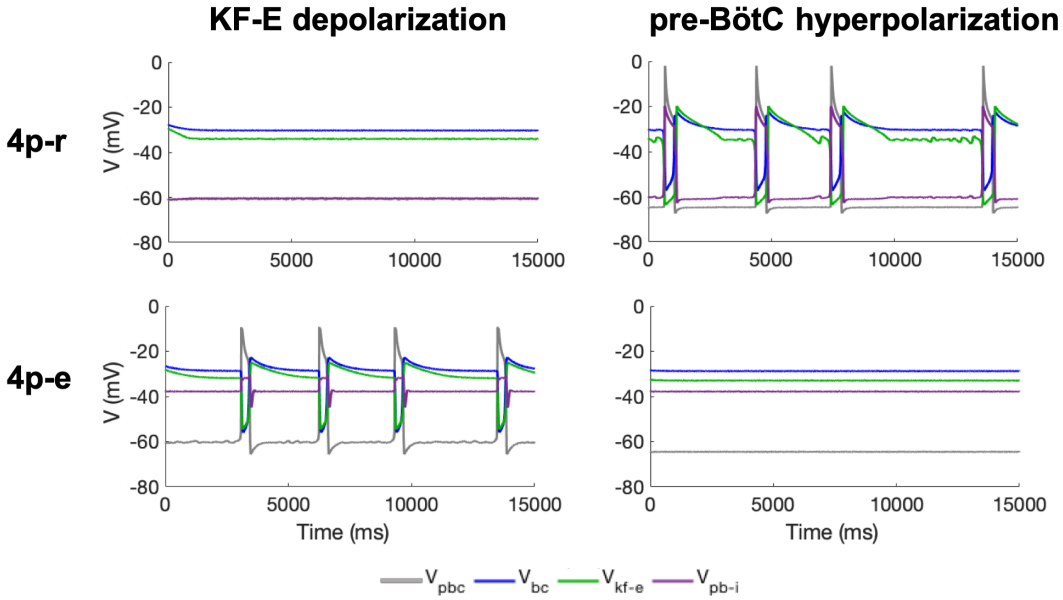

Figure 8: Stimulation experiments in RTT can distinguish the 4p-e and 4p-r models. Top row: Voltage time courses for the 4p-e model. Bottom row: Voltage time courses for the 4p-r model. Left column: Results of applying a small hyperpolarizing current to the pre-BötC unit. The 4p-e model predicts that this stimulation should pin the system in sustained apnea, whereas the 4p-r model predicts that this modulation should have little effect. Right column: Results of applying a small depolarizing current to the KF-E unit. The 4p-e model predicts that this stimulation should have little effect, whereas the 4p-r model predicts that this modulation should pin the system in sustained apnea. The legend explains the color codes for all panels.

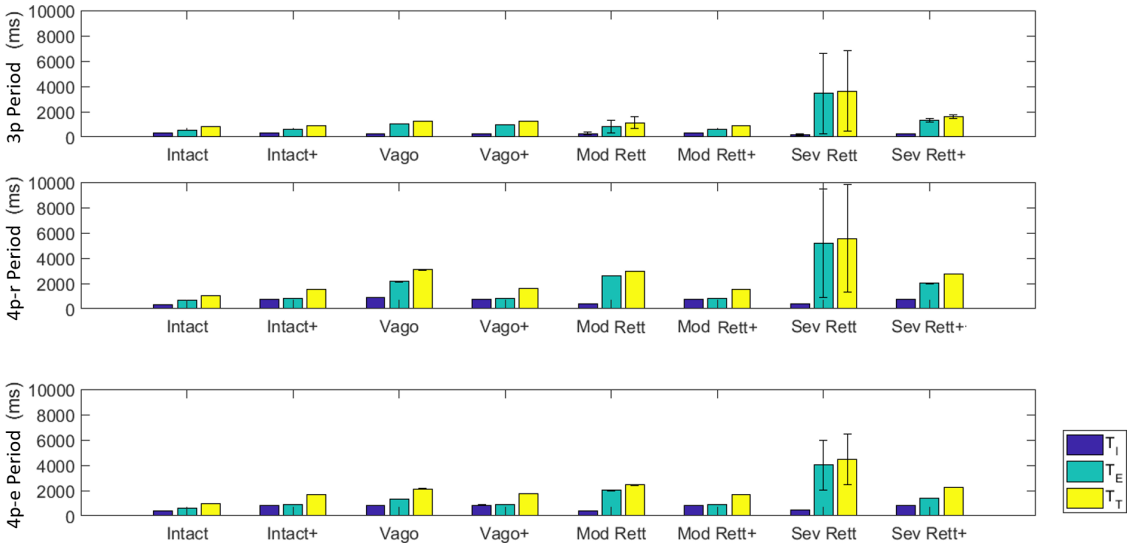

Figure 9: Breathing periods and standard deviations across all simulated regimes. Top: 3p model. Middle: 4p-r model. Bottom: 4p-e model. Navy blue bars: inspiratory phase duration (T_I). Aquamarine bars: expiratory phase duration (T_E). Yellow bars: Total period (T_T). Plus symbols denote simulated application of 5-HT$_{1A}$ agonist. For parameters used in the RTT cases shown here, see Table 8.

Table 1: Model neuron intrinsic behaviors

Tonic drive intact			
	3p	4p-r	4p-e
pre-BötC	Tonic at V = -37 mV	Tonic at V = -36 mV	Tonic at V = -35 mV
BötC	Oscillatory	Tonic at V = -39 mV	Tonic at V = -37 mV
KF-E	Tonic at V = -30 mV	Tonic at V = -35 mV	Tonic at V = -33 mV
KF-I		Tonic at V = -38 mV	Tonic at V = -38 mV
Tonic drive removed			
	3p	4p-r	4p-e
pre-BötC	Oscillatory	Oscillatory	Oscillatory
BötC	Quiescent at V = -60 mV	Oscillatory	Oscillatory
KF-E	Tonic at V = -30 mV	Tonic at V = -35 mV	Oscillatory
KF-I		Oscillatory	Oscillatory

Table 2: Shared parameters

conductances (nS)	reversal potentials (mV)	slope factors (mV)	other
$g_L = 2.8$	$E_L = -65.0$	$\sigma_h = 6.0$	$C = 21.0$ pF
$g_{syn-E} = 10.0$	$E_{Na} = 50.0$	$\sigma_m = -6.0$	$[S]_t = 0$ or 10 μM
$g_{syn-I} = 60.0$	$E_K = -85.0$		$\alpha = 1$
	$E_{syn-E} = 0.0$		
	$E_{syn-I} = -80.0$		

-10 cm-10 cm

Table 3: Non-synaptic 3p parameters

conductances (nS)		half activations (mV)		time constants (ms)	noise deviations (nA)	5-HT$_{1A}$ scaling factors
$g_{NaP_{pbc}} = 10$	$g_{KS_{pbc}} = 1$	$\theta_{h_{pbc}}$ = -50	$\theta_{\tau_{pbc}}$= -35	ϵ_{pbc}=400	$\gamma_{pbc} = 0.5$	$k_{\alpha 3_{pbc}} = 0.35$
$g_{NaP_{bc}} = 5$	$g_{KS_{bc}} = 0.3$	$\theta_{h_{bc}}$ = -50	$\theta_{\tau_{bc}}$= -25	ϵ_{bc}=1000	$\gamma_{bc} = 1$	$k_{\alpha 3_{bc}} = 1$
$g_{NaP_{kf-e}} = 10$	$g_{KS_{kf-e}} = 0.15$	$\theta_{h_{kf-e}}$ = -40	$\theta_{\tau_{kf-e}}$= -30	ϵ_{kf-e}=1750	$\gamma_{kf-e} = 1$	$k_{\alpha 3_{kf-e}} = 0.5$
$g_K = 0$		θ_m = -37				

Table 4: Synaptic 3p parameters

inhibitory synaptic scaling factors			
	pre-BötC	BötC	KF-E
pre-BötC		$b_{pbc,bc}$=0.0417	$b_{pbc,kf-e}$ = 0.0333
BötC	$b_{bc,pbc}$ = 0.0417		$b_{bc,kf-e}$ = 0.0083
excitatory synaptic scaling factors			
	pre-BötC	BötC	KF-E
pre-BötC		$a_{pbc,bc}$=0.11	
KF-E		$a_{kf-e,bc}$=1	
excitatory tonic scaling factors			
	pre-BötC	BötC	KF-E
pons	pd_{pbc}=0.55	pd_{bc}=0.11	pd_{kf-e}=0
medulla	med_{pbc}=0.45	med_{bc}=0.09	med_{kf-e}=0
synaptic half activations (mV)			
$\theta_{syn_{kf-e,bc}}$ = -10		$\theta_{syn_{j,i}}$ = -35 for all other j, i	
synaptic slopes			
$\sigma_{syn_{kf-e,bc}}$ = -8		$\theta_{syn_{j,i}}$ = -3 for all other j, i	
synaptic decay rates			
$\beta_{pbc,bc}$ = 0.005	$\beta_{pbc,kf-e}$ = 0.005	$\beta_{j,i}$ = 0.08 for all other j, i	

-10 cm-10 cm

Table 5: Non-synaptic 4p-r parameters

conductances (nS)		half activations slope factors (mV)		time constants (ms)	noise deviations (nA)	5-HT$_{1A}$ scaling factors
$g_{NaP_{pbc}}$ = 10	$g_{KS_{pbc}}$ = 1	$\theta_{h_{pbc}}$ = -47	$\theta_{\tau_{pbc}}$= -35	ϵ_{pbc}=600	γ_{pbc} = 1	$k_{\alpha 3_{pbc}}$ = 1
$g_{NaP_{bc}}$ = 5	$g_{KS_{bc}}$ = 1	$\theta_{h_{bc}}$ = -47	$\theta_{\tau_{bc}}$= -35	ϵ_{bc}=700	γ_{bc} = 1	$k_{\alpha 3_{bc}}$ = 1
$g_{NaP_{kf-e}}$ = 5	$g_{KS_{kf-e}}$ = 0.3	$\theta_{h_{kf-e}}$ = -40.25	$\theta_{\tau_{kf-e}}$= -35	ϵ_{kf-e}=1500	γ_{kf-e} = 1	$k_{\alpha 3_{kf-e}}$ = 0
$g_{NaP_{pb-i}}$ = 5	$g_{KS_{pb-i}}$ = 0.5	$\theta_{h_{pb-i}}$ = -47	$\theta_{\tau_{pb-i}}$= -35	ϵ_{pb-i}= 300	γ_{pb-i} = 1	$k_{\alpha 3_{pb-i}}$ = 0
g_K = 3.0		θ_m = -40.0	θ_{m_K} = -30.0			
			σ_{m_K} = -4.0			

Table 6: Synaptic 4p-r parameters

inhibitory synaptic scaling factors				
	pre-BötC	BötC	KF-E	PB-I
pre-BötC		$b_{pbc,bc}$=0.03	$b_{pbc,kf-e}$ = 0.1	
BötC	$b_{bc,pbc}$ = 0.035		$b_{bc,kf-e}$ = 0.001	
KF-E				$b_{kf-e,pb-i}$ = 0.05
PB-I			$b_{pb-i,kf-e}$ = 0.05	
excitatory synaptic scaling factors				
	pre-BötC	BötC	KF-E	PB-I
pre-BötC		$a_{pbc,bc}$=0.03		$a_{pbc,pb-i}$=0.15
excitatory tonic scaling factors				
	pre-BötC	BötC	KF-E	PB-I
pons	pd_{pbc}=0.15	pd_{bc}=0.5	pd_{kf-e}=0	pd_{pb-i}=0.8
medulla	med_{pbc}=0.15	med_{bc}=0.15	med_{kf-e}=0	med_{pb-i}=0
synaptic half activations (mV)				
	$\theta_{syn_{pb-i,kf-e}}$ = -30		$\theta_{syn_{j,i}}$ = -35 for all other j, i	
synaptic slopes				
	$\sigma_{syn_{pb-i,kf-e}}$ = -0.5		$\sigma_{syn_{j,i}}$ = -3 for all other j, i	
synaptic decay rates				
	$\beta_{pbc,bc}$ = 0.005	$\beta_{pbc,kf-e}$ = 0.005	$\beta_{j,i}$ = 0.08 for all other j, i	

-10 cm-10 cm

Table 7: Non-synaptic 4p-e parameters

conductances (nS)		half activations/ slope factors (mV)		time constants (ms)	noise deviations (nA)	5-HT$_{1A}$ scaling factors
$g_{NaP_{pbc}}$ = 10	$g_{KS_{pbc}}$ = 0.6	$\theta_{h_{pbc}}$ = -47	$\theta_{\tau_{pbc}}$= -35	ϵ_{pbc}=600	γ_{pbc} = 1	$k_{\alpha 3_{pbc}}$ = 1
$g_{NaP_{bc}}$ = 5	$g_{KS_{bc}}$ = 1.2	$\theta_{h_{bc}}$ = -47	$\theta_{\tau_{bc}}$= -35	ϵ_{bc}=800	γ_{bc} = 1	$k_{\alpha 3_{bc}}$ = 1
$g_{NaP_{kf-e}}$ = 5	$g_{KS_{kf-e}}$ = 2.5	$\theta_{h_{kf-e}}$ = -40.25	$\theta_{\tau_{kf-e}}$= -35	ϵ_{kf-e}=1500	γ_{kf-e} = 1	$k_{\alpha 3_{kf-e}}$ = 0
$g_{NaP_{pb-i}}$ = 5	$g_{KS_{pb-i}}$ = 0.5	$\theta_{h_{pb-i}}$ = -47	$\theta_{\tau_{pb-i}}$= -35	ϵ_{pb-i}=300	γ_{pb-i} = 1	$k_{\alpha 3_{pb-i}}$ = 0
g_K = 3.0		θ_m = -40.0	θ_{m_K} = -30.0			
			σ_{m_K} = -4.0			

Table 8: Synaptic 4p-e parameters

inhibitory synaptic scaling factors				
	pre-BötC	BötC	KF-E	PB-I
pre-BötC		$b_{pbc,bc}$=0.03	$b_{pbc,kf-e}$ = 0.2	
BötC	$b_{bc,pbc}$ = 0.0345		$b_{bc,kf-e}$ = 0.03	
PB-I			$b_{pb-i,kf-e}$ = 0.05	
excitatory synaptic scaling factors				
	pre-BötC	BötC	KF-E	PB-I
pre-BötC		$a_{pbc,bc}$=0.03		$a_{pbc,pb-i}$=0.15
KF-E		$a_{kf-e,bc}$=0.33		
excitatory tonic scaling factors				
	pre-BötC	BötC	KF-E	PB-I
pons	pd_{pbc}=0	pd_{bc}=0.35	pd_{kf-e}=0.6	pd_{pb-i}=0.8
medulla	med_{pbc}=0.3	med_{bc}=0.35	med_{kf-e}=0	med_{pb-i}=0
synaptic half activations (mV)				
	$\theta_{syn_{pb-i,kf-e}}$ = -33		$\theta_{syn_{j,i}}$ = -35 for all other j, i	
synaptic slope factors (mV)				
	$\sigma_{syn_{pb-i,kf-e}}$ = -0.5		$\sigma_{syn_{j,i}}$ = -3 for all other j, i	
synaptic decay rates				
	$\beta_{pbc,bc}$ = 0.005	$\beta_{pbc,kf-e}$ = 0.005	$\beta_{j,i}$ = 0.08 for all other j, i	

Table 9: RTT parameters

3p			
	$b_{pbc,kf-e}$	$b_{bc,kf-e}$	
Intact	0.0333	0.0083	
Mod RTT	0.02	0.003	
Sev RTT	0	0.001	
4p-r			
	$b_{pbc,kf-e}$	$b_{bc,kf-e}$	$b_{pb-i,kf-e}$
Intact	0.1	0.001	0.05
Mod RTT	0.032	0.00032	0.0398
Sev RTT	0	0	0.035
4p-e			
	$b_{pbc,kf-e}$	$b_{bc,kf-e}$	$b_{pb-i,kf-e}$
Intact	0.2	0.03	0.05
Mod RTT	0.1	0.015	0.0375
Sev RTT	0	0	0.025